”DEVELOPMENT OF A HIGH-POWER PULSED LASER via SUM-FREQUENCY GENERATION FOR SODIUM LIDAR APPLICATIONS”

by

CHRISTIANE A. EBONGUE

A THESIS

Submitted in partial fulfillment of the requirements
for the degree of Master of Science in the
Natural Resources Graduate Program
of Delaware State University
DOVER, DELAWARE
May 2019

This thesis is approved by the following members of the Final Oral Review Committee:

Dr. Renu Tripathi, Committee Chairperson, Division of Physical & Computational Sciences, Delaware State University

Dr. Gour Shyam Pati, Committee Member, Division of Physical & Computational Sciences, Delaware State University

Dr. Yuriy Markushin, Committee Member, Division of Physical & Computational Sciences, Delaware State University

Dr. Qiquan Wang, External Committee Member, Department of Chemistry, Delaware State University

DEDICATION

To Samuel (Ike) Faddis. I cannot express with words my indebtedness to you. Thank you for handling the way you do, my mood swings, my frustrations, and my successes. You are my blessing from heaven.

ACKNOWLEDGEMENT

First, I would like to thank my adviser, Dr. Renu Tripathi for giving me the opportunity to work and learn in her laboratory. The challenges I faced, the mistakes I made, all contributed in my maturity, and I can say with confidence that it was worth working under your supervision. I would also like to say a special thanks to Dr. Gour Pati. Every time I knock in your office, I usually say that it will only take 5 min. But deep down you already know it will take half an hour or more. However, you always have time to answer my questions or help me with whatever issue I have in the lab. Thank you! My gratitude also goes to you, Dr. Raghwinder Singh Grewal (Raghu). I really appreciated that whenever I would call your name, your first reaction would be ”yes please tell how I can help.” Thank you very much for your kind inputs for the past couple of months and even though it was short, I enjoyed working with you. I would also like to thank my committee members, Dr. Yuriy Markushin, and Dr. Qiquan Wang, for their time, and valuable remarks concerning my thesis.

To my friends and especially my dearest friends, Oluchi, David, Jennifer, Peter, Kenny, and Karol. We may not talk or see each other very often, but every time I pick up the phone to reach out to you for help, whether is for a physics related problem or with help moving, or just to talk about something that made me upset, you jump from your sit to come to my rescue. I hope you know you have a particular place in my heart. Ivan Gusachenko, you are quite a funny guy but so resourceful. For the past two-years, the time you took to chat with me about science or even given me simple advises about life, I can only wish to be as kind as you.

To Dr. Luis Orozco, Pablo Solano, and Jeff Grover, you cannot possibly imagine how much impact you have or have made in my life. The time I spent working with you is truly what is pushing me to keep going. I loved research before but now, I am in love with research because

of you. Your love for science and knowledge is palpable and one of my secret dreams is to be able to discus Physics related topics with you all again. In a meantime, I will keep sharpen my skills to get to your level of inspiration.

Now my family ... mom and sis (Julia), you both are my role models. I am such a lucky ’brat’ to have you in my life. Your supports, your dedications in raising me to become an independent woman, and your love, have made me who I am today. I know I do not say it much but I truly love you. To Linda, and Audrey, to my aunties, Patience, and Lydienne – What can I say. You gals are my amazing women-heroes. For the past decades, whenever ”hell comes loose”, I know I have you as my backbone and I want to say thank you for the love, support and help you have given me throughout my education, as well as personally. You somehow always know what to say to keep pushing me forward in life.

ABSTRACT

We present the development of a nanosecond pulsed laser system resonating at sodium wavelength (589 nm) by means of sum frequency generation (SFG) with Nd:YAG lasers at 1064 nm and 1319 nm. This research is aimed to perform lidar measurements at mesospheric altitude, using sodium atoms as the tracer. These measurements include the determination of the sodium density, temperature and radial velocity. Two high power lasers at 1064 nm and 1319 nm are constructed using commercially available Nd:YAG gain modules as building blocks. The radiations emitted by the diode pumped Nd:YAG gain modules are picked up by two respective hemispherical optical cavities designed with high reflective mirrors at 1064 nm and 1319 nm, to produce stimulated emission at each wavelength. The 589 nm laser radiation is obtained by the sum frequency generation (SFG) of the two Nd:YAG pump laser outputs in a nonlinear crystal. Perfect mode matching, beam overlap, as well as temporal overlap of Q-switched pump laser pulses are ensured to achieve optimum frequency conversion in the SFG crystal. Precise tuning of the laser wavelength to the sodium D2 line is achieved by injection seeding of the 1064 nm pump laser with a single-frequency DFB laser. We have studied the performance of this laser for sodium lidar applications.

Keywords: Q-switching, frequency mixing, injection seeding, optical resonators

TABLE OF CONTENTS

1 Introduction **1**

1.1 Relevance of Sodium LiDAR 1

1.2 Sodium Laser Technology 2

1.3 Sum Frequency Sodium Laser 3

1.4 Outline of thesis 6

2 Laser Resonator and Gain Module Assembly **8**

2.1 Resonator: Concept and Design 8

2.1.1 Concept 8

2.1.2 Simulation 15

2.1.3 Design 19

2.2 Nd:YAG Gain Medium 21

2.3 Laser System Assembly 25

2.3.1 Chiller for Laser Cooling 26

2.3.2 Installation of Gain Module 26

2.3.3 Optical Cavity Alignment 29

3 Laser Characterization **32**

3.1 Power Scaling 32

3.2 Power Stability 36

3.3 Beam Characterization 39

3.3.1 Beam Profile 39

3.4 Long Pulse Characterization 43

3.4.1 1064 nm Laser Pulses 43

4 Short-Pulse Generation: Q-Switching 47

4.1 Pockels' Cell 48

4.2 Q-Switch YAG Lasers 51

4.3 Limitations of Q-switching (Mode Locking) 60

5 Sum-Frequency Generation at 589 nm 61

5.1 Sum-Frequency Conversion (SFG) 61

5.2 High Power SFG 65

5.3 Low Power SFG 67

5.4 Injection Seeding 69

6 Sodium Laser Design: Alternate Approach 70

6.1 Second-Order Harmonic Generation (SHG) 70

6.2 Quasi-Phase Matching for high-efficiency SHG 72

6.3 SHG-TA/DFB Laser System 73

7 Conclusion and outlook 80

LIST OF TABLES

1.1 Requirements for Sodium LiDAR 2

2.1 Cavity Geometrical Parameters 16
2.2 Resonators mirror' parameters for 1064 nm and 1319 nm pump laser 20
2.3 Nd:YAG Laser Parameters 25
2.4 Nd:YAG Material Parameters 25
2.5 Nd:YAG gain module operating limits 27

3.1 Fitting Parameters for 1064 nm 34
3.2 Fitting Parameters for 1319 nm 34
3.3 Fitting Parameters for 1319 nm & slope efficiency 34
3.4 Energies values for 1064 nm 35
3.5 Energies Values for 1319 nm 35
3.6 Fundamental properties of the laser beam 43
3.7 Duty Cycle in terms of current pulse widths 45

4.1 Physical parameters for BBO and KDP Crystals 51
4.2 Gaussian fitting parameters 57
4.3 Gaussian fitting parameters 59

5.1 Uniaxial Crystals' Phase Matching Conditions 64
5.2 Cavity Geometrical Parameters 65

LIST OF FIGURES

2.1 Two-mirror planar resonator 9

2.2 Resonance frequencies for different cavity length 11

2.3 Stability Diagram of hemispherical optical resonator 16

2.4 Basic components of a hemispherical optical resonator 17

2.5 Stability map as a function of radius of curvature 18

2.6 Variation of the beam size along the optical cavities 19

2.7 Optical cavity design implemented in the experimental set-up 19

2.8 Optical cavity set-up for 1064 nm and 1319 nm 20

2.9 Energy-level diagram of an Nd:YAG laser 22

2.10 Population inversion of a four energy-level system 23

2.11 Gain along an optical cavity 24

2.12 Chiller's front and back panels 26

2.13 Gain Module for either 1064 nm or 1319 nm pump lasers. 27

2.14 Basic illustration of the gain module connections 28

2.15 eDrive controller and power supply for 1064 nm laser 28

2.16 Demonstration of the 808 nm fluorescence caused by optical pumping 29

2.17 Setup of both laser resonators, 1064 nm and 1319 nm 30

2.18 Resonator alignment setup 30

2.19 Back reflections caused by the 1064 nm cavity misalignment 30

3.1 Power scaling of 1064 nm pump laser 33

3.2 Power scaling of 1319 nm pump laser 33

3.3 1319 nm pump laser power scaling above 50 Amps at 300 Hz 35

3.4 1319 nm pump laser demonstrating power instability 37
3.5 1064 nm pump laser power stability 37
3.6 1319 nm pump laser power stability 38
3.7 Beam Profiler 42
3.8 2D intensity distribution of the 1064 nm laser 42
3.9 Output current pulse of 1064 nm laser 44
3.10 1064 nm laser pulses at different pulse widths 45
3.11 1064 nm laser pulses at different currents 46

4.1 General configuration of a cavity resonator with a Q-switch 48
4.2 General configuration of a cavity resonator with a Q-switch 50
4.3 Q-Switched Pulse Lasers 51
4.4 1064 nm laser cavity Q-Switching configuration 52
4.5 1319 nm laser cavity Q-Switching and alignment configuration 53
4.6 Timing diagram for 1064 nm and 1319 nm pump lasers 54
4.7 Time delay set up 54
4.8 Demonstration of after pulses obtained from cavity misalignment 56
4.9 Ringing caused by timing error 56
4.10 A Q-switched pulse from the 1064 nm YAG laser 57
4.11 Q-switch pulse from the 1064 nm YAG laser fitted to a Gaussian 58
4.12 Power stability of the Q-switched 1064 nm YAG laser 58
4.13 A Q-switch pulse from the 1319 nm YAG laser 59
4.14 Q-switch pulse from the 1319 nm YAG laser fitted to a Gaussian 59

5.1 Illustration of sum-frequency generation in a nonlinear crystal 62
5.2 Sodium laser Schematic 66
5.3 Top and bottom configuration of the 1319 nm laser diode mount 68

5.4 Laser diode controller, front and back panels 68

5.5 Waveguide SFG: 1064 nm + 1319 nm 68

5.6 Temperature tuning of the 1064 nm DFB laser in terms of SFG output power . . . 69

5.7 Temperature tuning of the 1064 nm DFB laser in terms of wavelength 69

6.1 Schematics of CW Sodium Laser 74

6.2 Tapered amplifier connections 75

6.3 PPLN crystal physical structure 75

6.4 Temperature tuning of the CW laser system 76

6.5 Seed power before and after fiber isolator 77

6.6 Temperature tuning of seed laser 77

6.7 Low power CW set-up 78

6.8 Low power CW set-up 79

CHAPTER 1

INTRODUCTION

The Earth's atmosphere, particularly its upper layer, the Mesosphere, is composed of a diverse range of neutral atoms that essentially lie within the spectrum of metallic atoms in the periodic table. For instance, alkali metal atoms such as sodium (Na) and potassium (K), transition metals like iron (Fe), and alkaline earth metals such as magnesium (Mg) and calcium (Ca) are the most predominant atoms in this layer of the atmosphere [1]. The appearance and subsistence of these atoms in the Mesosphere is caused by the perpetual disintegration of dust particles originating from collisions of interplanetary objects with Earth's atmosphere [2]. In recent years, laser technology has enabled the development of ground-based experimental studies of the Mesosphere by investigating wind and temperature affects on the mentioned atoms. Sodium atoms are of particular interest because the sodium light on resonance to its D_1 or D_2 transition line, has a narrow linewidth that permits experiments 100 km above ground without any influence or interaction with other atomic layers in the Troposphere, Stratosphere or Mesosphere. In this chapter, the relevance of Sodium LiDAR and its technology are described in detail.

1.1 Relevance of Sodium LiDAR

The boundary of the Mesosphere is approximated to be between 60 to 110 km above ground [3] and it is a constant subject of perturbations caused by either the periodic oscillation of the atmosphere, the dynamics of gravitational waves (GW) or by the occurrence of atmospheric Rossby waves, also known as planetary waves [4]. Unfortunately, past methods employed to understand the impact of these phenomenon on Earth's atmosphere have produced limited information to produce detailed characterization of temperature and wind profiles of the Mesosphere. These previous methods include falling spheres and airglow observations [5, 6]. In the 90s, She et al. achieved high-resolution measurements of both temperature and wind profiles of the mesosphere by implementing a two-frequency LiDAR technique in which the laser is tuned on resonance to the sodium atoms to detect dynamical changes in Na atoms [7] hence, providing valuable information on the basic structure of the Mesosphere.

Wavelength	589.159 nm (in Vacuum)
Optical Power @ 589 nm	2-5 W
Pulse	Yes
Pulse duration	1 - 50 ns
Spectral Width	$<$ 100 MHz
Beam quality (M^2)	$<$ 4

Table 1.1: Requirements for Sodium LiDAR

After several years of implementing LiDAR systems that use Na atoms as the tracer, it has been proven that sodium LiDAR technique is capable of providing accurate information of the composition and fluctuations of the Mesosphere, in both ground-based and airborne surveillance. The aim of our Sodium LiDAR is to contribute to this comprehensive analysis on the influence that phenomenon such as GW and others stated earlier, have on our atmosphere. The basic requirements of the sodium LiDAR laser are listed in table 1.1.

1.2 Sodium Laser Technology

To conveniently perform wind and temperature measurements via Sodium LiDAR, several techniques have been implemented to obtain the desired coherent sodium light. For instance, H. Friedman et al. reported in 1995 their 20 W sodium guide-star laser by using dye lasers as the pump [8]. More recently, in 2004, S. Rabien et al. also reported obtaining power of about 20 W from a cw single frequency dye laser at 589 nm [9]. Further well known techniques have implemented fiber Raman lasers. Fiber Raman lasers have the advantage of being tunable in a large-scale of wavelengths that are not readily available with common manufactured lasers. Powerful Raman fiber amplifier lasers have been reported by [10, 11, 12].

A now well-established approach of obtaining the 589 nm laser is based on propagating or mixing solid-state infrared lasers in nonlinear media. Jeys et al reported in 1989 the generation of high power pulsed sodium laser by sum-frequency mixing two neodymium yttrium aluminum garnet (Nd:YAG) lasers with wavelength at 1060 nm and 1319 nm, respectively [13]. Since then, solid-state infrared lasers have been frequently implemented in systems that aim to generate the sodium resonance radiation. The sodium laser presented in this thesis is obtained by mixing the output of Nd-YAG lasers operating at wavelengths 1064 nm and 1319 nm, respectively. It should be noted that there are drawbacks from utilizing techniques involving dye lasers or Raman fiber. In the case of dye lasers for instance, the laser cavity length must be extremely lengthy (15 m long) in order to obtain the desired spectral coverage of the sodium spectrum [13]. The nonlinear sum-frequency of all-solid-state lasers has shown to be more compact with high conversion efficiency of 589 nm, and improved beam quality [14].

1.3 Sum Frequency Sodium Laser

As already stated, the all-solid state sum frequency sodium laser relies on the nonlinearity of the crystal used for the frequency conversion. The frequency conversion in turn, depends on the presence of light with a strong intensity such that the internal properties of the nonlinear crystal are forced to change [15]. To have a better understanding of the sum frequency sodium laser, it is important to understand the nonlinear processes it is built upon.

The crystals used for sum frequency conversion are said to exhibit birefringence, a phenomena in which the refractive index of a crystal depends on the propagation and polarization of the light field [16]. In a nonlinear crystal, as compared to a linear one, the characteristics of an electromagnetic wave are strongly dependent on the polarization of the electric field propagating inside the nonlinear medium. If $\mathbf{P} = \varepsilon_0 \chi^{(1)} \mathbf{E}$ in a linear material, the vector form of the polarization in a nonlinear material is given as,

$$\begin{aligned} \mathbf{P} &= \varepsilon_0 \chi^{(1)} \mathbf{E} + \varepsilon_0 \chi^{(2)} \mathbf{EE} + \varepsilon_0 \chi^{(3)} \mathbf{EEE} + ... \\ &= \mathbf{P}_L + \mathbf{P}_{NL} \end{aligned} \tag{1.1}$$

where $\chi^{(1)}$, $\chi^{(2)}$, $\chi^{(3)}$ are the first, second and third order susceptibility tensors, and ε_0 is the free-space permittivity. Note that the expressions, **EE**, **EEE** are not dot products but rather tensors quantities, such that the entire expression is a vector quantity. $\mathbf{P}_{NL}$ represents the polarization terms for nonlinear processes.

A useful representation of the polarization that helps to understand fundamental processes occurring in nonlinear media is its scalar form, in which only the amplitude of the electric field is considered as such:

$$\begin{aligned} P &= \varepsilon_0 \chi^{(1)} E + \varepsilon_0 \chi^{(2)} E^2 + \varepsilon_0 \chi^{(3)} E^{(3)} + ... \\ &= P_L + P_{NL} \end{aligned} \tag{1.2}$$

the second term of equation 1.2 describes any second-order effects of the polarization. The third-term is related to third-order processes, which are not considered in the scope of this thesis. It is important to note that while $\chi^{(1)}$ is dimensionless, $\chi^{(2)}$ has units of meter per volts ($\frac{m}{V}$) due to the quadratic term of the electric field.

There are several types of nonlinear crystals, categorized as uniaxial, and biaxial crystals. These crystals are capable of splitting an incident beam of light into two refracted beams that propagate in two different axes of the crystal, called ordinary and extraordinary axis. Considering a uniaxial crystal with a set of principle coordinate axes, x, y and z such that the linear relation between displacement D and the electric field E, ($\frac{D_i}{\varepsilon_0} = \varepsilon'_{ij} E_j$) is written as:

$$D_x = \varepsilon_0 \varepsilon_{11} E_x \tag{1.3}$$

$$D_y = \varepsilon_0 \varepsilon_{22} E_y \tag{1.4}$$

$$D_z = \varepsilon_0 \varepsilon_{33} E_z \tag{1.5}$$

Note that ε'_{ij} and ε_{ij} are different. The former represents the initial axes of the crystal. In comparison to isotropic crystals which have $\varepsilon_{11} = \varepsilon_{22} = \varepsilon_{33}$, uniaxial and biaxial crystals have the following properties, $\varepsilon_{11} = \varepsilon_{22} \neq \varepsilon_{33}$, and $\varepsilon_{11} \neq \varepsilon_{22} \neq \varepsilon_{33}$, respectively. Uniaxial crystals are the focus of this study.

For a propagating electromagnetic wave in the XY-plane of a uniaxial crystal such that the displacement $\mathbf{D}$ is expressed as $\mathbf{D} = \varepsilon_0 \varepsilon_{11} \mathbf{E}$ The speed of propagation of this wave in the ordinary axis of the crystal is then:

$$v_o = \frac{c}{\sqrt{\varepsilon_{11}}} = \frac{c}{n_o} \tag{1.6}$$

where $n_0 \equiv \varepsilon_{11}$ is the refractive index in the ordinary axis of the crystal, also known as the optic axis. In this case, the z-axis represents the optic axis and the electric field of the wave is always orthogonal to this axis. If on the other hand, the displacement $\mathbf{D}$ is expressed as $\mathbf{D} = \varepsilon_0 \varepsilon_{33} \mathbf{E}$, the speed of the wave is now,

$$v_e = \frac{c}{\sqrt{\varepsilon_{33}}} = \frac{c}{n_e} \tag{1.7}$$

where n_e is the index of refraction the wave sees when traveling in the extraordinary axis of the crystal. In summary, there are two polarization axes that characterize a nonlinear crystal, the o and the e polarization, for ordinary and extraordinary axis, respectively. A general representation of the refractive index seen by a wave traveling at an angle θ with respect to the optic axis in a uniaxial crystal is given by:

$$\frac{1}{n^2(\theta)} = \frac{cos^2(\theta)}{n_o^2} + \frac{sin^2(\theta)}{n_e^2} \tag{1.8}$$

Compact sum-frequency sodium lasers have been obtained via the mixing of two infrared Nd-YAG gain media within crystals such as a periodically poled $KTiOP_4$ crystal [17], a potassium titanyl phosphate (KTP) crystal [14] etc. There are two methods of obtaining a sodium laser, by either intra-cavity or extra-cavity sum frequency generation (SFG). In the intracavity SFG, the crystal sits within the optical cavity and the output power P_3 of the generated yellow light with wavelength λ_3 is given by:

$$P_3 = \alpha P_1 P_2 \tag{1.9}$$

where P_1, P_2 are the intra-cavity power of the pump lasers which are approximated to be weakly-depleted pump lasers. Evidently, the conversion efficiency of SFG is restricted by the weakest of the pump lasers (P_2) [17], such that the obtained maximum photons output at λ_3 is equal to the input photons at λ_2 such that

$$P_3^{(max)} = \left(\frac{\lambda_2}{\lambda_3}\right) P_2 \tag{1.10}$$

Shi has reported generation of 5 Watts of sodium light by mixing 11 Watts of 1064 nm pump laser and 9 watts of 1319 nm pump light [18].

1.4 Outline of thesis

This thesis is divided into a series of concepts and experimental set-up. Chapter II is a highlight of the basic aspects of optical resonators but also a detailed description of the laser systems assembly I have spent a considerable amount of time on. In Chapter III, I have characterized each pump lasers used to obtain the sodium laser. The characterization of the lasers includes power scaling, power stability, and beam profiling. The micro-pulse output of each laser is also described.

Chapter IV demonstrates the scheme used to obtained short laser output pulses and examines the short-pulse generated via Q-switching. A short section on the limitation of Q-switching is also discussed. Finally, within the scope of sum-frequency generation, I present the details of the sum-frequency sodium laser for LiDAR application. Section VI is an extra section concerning the first experiment I have worked on during my Master, based on the design of a frequency doubled 589 nm laser for laboratory experiment.

CHAPTER 2

LASER RESONATOR AND GAIN MODULE ASSEMBLY

2.1 Resonator: Concept and Design

The principle of a laser resonator is similar to the familiar electrical or mechanical resonators commonly used, such as an LC circuit, a mass on a spring, or even a simple pendulum. These resonators are characterized by the oscillation frequency predetermined by the configuration of the system. In the case of a simple pendulum for instance, only a single frequency component given by $f = \frac{1}{2}\sqrt{g/l}$, can be sustained during its period of oscillation, where g and l represent the gravitational constant and pendulum's length, respectively. The frequencies at which a resonator oscillates are therefore called resonance frequencies. The question that comes to mind is, how does one construct and characterize a resonator for light, also referred to as optical cavity. In this chapter, a brief description on the concept behind optical resonators is presented and the design of a two-mirror hemispherical optical resonator is described in detail.

2.1.1 Concept

There are several techniques used to build a laser resonator. One could either implement a two-mirror cavity system, a ring cavity resonator, or a whispering gallery resonator etc. However, each of these optical resonators are built with the same three components: an active medium which acts as an amplifier, a pumping system, and an optical feedback system, The amplifier in laser optics is known as the active medium of the resonator.

Optical resonators are characterized by the following: the feedback and spatial confinement they provide as the light bounces back and forth within the cavity, the quality factor (Q) of the resonator, and the photon lifetime (the time it takes for a photon of light to escape the cavity). This section does not aim to go over every detail of optical resonators, but rather to discuss their key features. Therefore, concepts such as cavity resonance frequency, free spectral range (FSR), quality factor of a laser resonator, and photon lifetime of a two-mirror optical resonator are introduced.

There are distinct configurations of a two-mirror resonator which are categorized as planar, hemispherical, and spherical. We have used the hemispherical-mirror configuration to construct our optical resonators. However, to get an intuition of the fundamental concepts of these optical resonators, a model of a planar resonator is used, as it is the simplest of the family of resonators.

A two-mirror planar resonator as the name suggests, consists of two plane parallel mirrors separated by a distance L_0. One common example of this resonator is known as a Fabry-Perot resonator [19]. Consider an initial wave $\mathbf{E}_0$ with zero phase, travelling within the optical cavity shown in figure 2.1. The wave is repeatedly reflected off of mirrors M_1 and M_2. Each time it

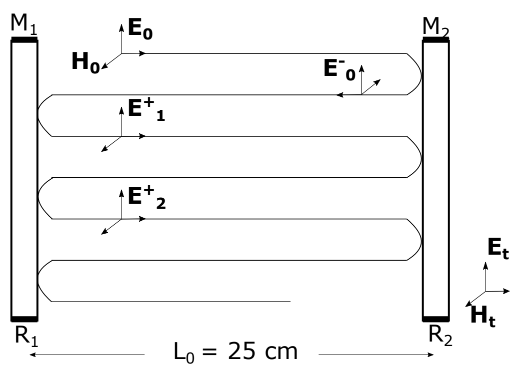

Figure 2.1: Two-mirror planar resonator

returns to the starting position it has acquired some phase shift relative to the initial beam. $\mathbf{E}_1$ and $\mathbf{E}_2$ represent the electric fields of different reflected beams at the same position. In order for the various electric fields of these reflected beams to interfere constructively, the spacing of the mirrors must be an integer multiple of the wavelength such that the round trip phase shift is an integer multiple of 2π. A round-trip of a wave therefore corresponds to twice the distance (L_0) between the mirrors, and the round-trip phase shift (RTPS) is expressed as:

$$RTPS = k2L \tag{2.1}$$

where the wavenumber k is equal to,

$$k = \frac{n\omega}{c} \tag{2.2}$$

ω is the angular frequency of light, and c is the speed of the wave inside the cavity ($c = \frac{c_0}{n}$). The refractive index of the medium, n, is assumed to be unity.

The RTPS can also be expressed in terms of frequency using equation 2.2, as follows:

$$RTPS = k2L_0 = \left(\frac{n\omega}{c}\right)2L_0 = \frac{4\pi n\nu L_0}{c} \tag{2.3}$$

where ν represents the resonance frequency of the cavity. As mentioned, the last equality of equation 2.3 shows that a cavity resonance occurs when the RTPS is an integer multiple of 2π. Therefore, we can write the following relationship:

$$RTPS = k2L_0 = q2\pi \tag{2.4}$$

where q is an integer number (q = 1, 2, ...) representing the number of cavity resonance frequencies, also known as cavity modes, an optical resonator can have. Expressing the cavity length L_0 using equations 2.3 and 2.4, in terms of the resonance frequency ν gives:

$$2L_0 = \frac{qc}{n\nu} \tag{2.5}$$

or equivalently in terms of wavelength,

$$2L_0 = q\lambda \tag{2.6}$$

where $\lambda_0 = n\lambda$.

Equation 2.6 shows that there are integer number of wavelengths created along the cavity in one round-trip. Consequently, there are several discrete resonance frequencies (ν_q) or wavelengths (λ_q) which are allowed within a laser resonator. Cavity resonance frequencies are also known as longitudinal modes [20] and the separation between these modes is described by the free spectral range (FSR), written as:

$$FSR = \nu_q - \nu_{q+1} = \frac{c}{2nL_0} \tag{2.7}$$

Figure 2.2 illustrates the behavior of the resonance frequencies for different cavity lengths. As the distance between the mirrors increases, the spacing between the resonance frequencies decreases. Therefore, one way to reduce the number of resonance frequencies within a cavity, is to increase the cavity length. As an example, consider a radiation of 1064 nm in wave-

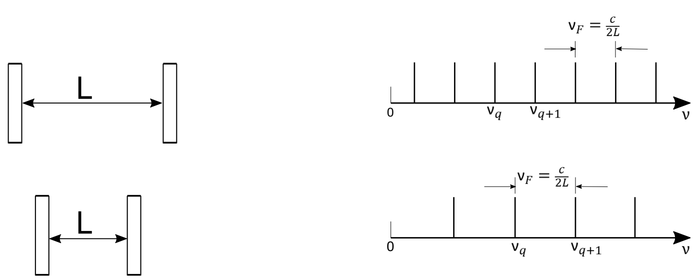

Figure 2.2: Resonance frequencies for different cavity length

length propagating within the given planar optical cavity of length $L_0 = 25 \;\; cm$. The mode number q within the cavity is found to be $q = \frac{2L}{\lambda} \approx 10^7$. The spacing between these resonance frequencies is then, $\nu_F = \frac{c}{2L} \approx 600 \;\; MHz$.

We have discussed the cavity resonance of an optical resonator and have seen that compared to electrical or mechanical resonators, an optical resonator can have several resonance frequencies based on the geometrical property of the resonator. Though it has not yet been mentioned how the initial electric field $\mathbf{E}_0$ is supplied, the field inside the optical cavity of figure 2.1 can still be described. The total internal electric field of all the fields propagating in the same direction as $\mathbf{E}_0$, is denoted $\mathbf{E}_t^+$, and is represented by:

$$E_T^+ = \sum E_N^+ = \mathbf{E}_0 \left[1 + A_1 \cdot A_2 e^{-ik2L_0} + (A_1 \cdot A_2 e^{-ik2L_0})^2 + ...\right] \tag{2.8}$$

The second term, $E_0(A_1 A_2 e^{-ik2L_0})$, describes the first round trip of the light inside the cavity. The third term is related to its second round trip and so forth. In terms of the optical cavity distance, $d = \frac{\omega n_0}{c}$, one obtains,

$$E_t^+ = \mathbf{E}_0 \left[\frac{1}{1 - A_1 \cdot A_2 e^{-i2d}}\right] \tag{2.9}$$

where $A_1 \cdot A_2$ is the amplitude change the wave experiences after each round trip, and e^{-ik2L_0} is the phase factor gained after one round-trip. Similarly, there is a total electric field E_t^- that is traveling to the left from M_2 and is defined as:

$$E_t^- = A_2 e^{-i2d} E_T^+ = \mathbf{E}_0 \left[\frac{A_2 e^{-i2d}}{1 - A_1 \cdot A_2 e^{-i2d}}\right] \tag{2.10}$$

It should be noted from equation 2.9 and 2.10 that both fields, E_t^+ and E_t^-, reach their maximum values when the denominator is a minimum which once again, implies that the fields resonance is obtained if $2d = q2\pi$, which is the same condition derived in equation 2.4

The intensities of each field, E_t^+ and E_t^-, are obtained by considering that the intensity of light is proportional to the square of the electric field as $(\frac{E \cdot E^*}{2\eta})$. Assuming a reference point (z=0) to the right of the surface of M_1, the intensity I^+, related to E^+, is then given by:

$$I^+(z=0) = \frac{|\mathbf{E}_0|^2}{2\eta}\left[\frac{1}{1 - A_1 \cdot A_2 e^{-i2d} - (A_1 \cdot A_2 e^{-i2d})^* + |A_1 \cdot A_2|^2}\right] \tag{2.11}$$

Simplifying this equation in terms of sine and cosine terms, we get:

$$I^+(z=0) = I_0\left[\frac{1}{1 - 2|A_1 \cdot A_2|[1 - 2\sin^2 d] + |A_1 \cdot A_2|^2}\right] \tag{2.12}$$

Furthermore assuming the field reflection coefficients are real values, we can then use the fact that the power reflection coefficient of each mirror $R_{1,2}$ is equal to the square of the absolute value of the field amplitude ($R_{1,2} = |A_{1,2}|^2$) and substitute $R_{1,2}$ into equation 2.12 to obtain,

$$I^+(z=0) = \frac{|E_0|^2}{2\eta}\left[\frac{1}{(1-\sqrt{R_1R_2})^2 + 4\sqrt{R_1R_2}\sin^2 d}\right] \tag{2.13}$$

$\frac{|E_0|^2}{2\eta}$ is simply an intensity and is equal to $T_1 \cdot [\frac{E_{inc}^2}{2\eta}]$. For any lossless mirrors, $T_1 = 1 - R_1$. Then,

$$I_t = \left[\frac{E_0^2}{2\eta} = T_1 I_{inc} = (1-R_1)\, I_{inc}\right]\left[\frac{T_2 = (1-R_2)}{(1-\sqrt{R_1R_2})^2 + 4\sqrt{R_1R_2}\sin^2 d}\right] \tag{2.14}$$

$$T(d) = \frac{I_{trans}}{I_{inc}} = \frac{(1-R_1)(1-R_2)}{(1-\sqrt{R_1R_2})^2 + 4\sqrt{R_1R_2}\sin^2 d} \tag{2.15}$$

To obtain a laser and to enable analyses of the laser output light, one of the mirrors, referred to as output coupler (OC), has to be partially reflective such that light bouncing inside the cavity can be transmitted after N number of round-trips. As a consequence of using a partially reflective mirror, a propagating wave within the cavity decays with time. This decay is expressed in terms of the photon lifetime, t_c, and it is the average time a propagating wave (or photon) bounces back and forth between the mirrors before it escapes the cavity. Let N_p be the initial number of photons within the cavity, and S the number of photons surviving one round trip such that, $N_{lost} = [1-S]N_p$, is the number of photon lost in a round trip. The rate of change, $\frac{dN_p}{dt}$, of photons within the cavity is then given by:

$$\frac{dN_p}{dt} = -\frac{[1-S]N_p}{2L_0} \tag{2.16}$$

where,

$$\tau_p = \frac{2L_0}{1-S} \tag{2.17}$$

is known as the photon lifetime. The parameter S is referred as the cavity survival factor, and $2L_0$ is the round-trip distance.

In the preceding paragraphs, it is found that the resonant cavities have a narrow band of oscillation frequencies. A particular cause of the appearance of these discrete frequencies is related to the dissipation of energy in the cavity walls or in any dielectric material within the cavity. The quality (Q) factor is a measure of the sharpness of a resonance frequency. It is defined as the ratio of the time-averaged energy stored in the cavity to the energy loss per cycle [21]:

$$Q = \omega_0 \frac{Stored\ \ energy}{Power\ \ loss} \tag{2.18}$$

where ω_0 is the resonance frequency if no loss is assumed. In terms of the resonance frequency ν_q of the cavity, the Q factor is given as,

$$Q = \frac{\nu_q}{\Delta\nu_{1/2}} \tag{2.19}$$

where ν_q is the frequency of one of the cavity peak frequencies and $\Delta\nu_{1/2}$ is the full width at half of the maximum (FWHM). Because the numerical values of the Q factor for optical frequencies could be quite large, another way to describe the sharpeness of a resonance frequency is through another quantity known as the Finesse (F).

$$F = \frac{free\ \ spectral\ \ range}{FWHM} = \frac{c/(2nd)}{\Delta\nu_{1/2}} \tag{2.20}$$

or

$$F = \frac{\pi(R_1R_2)^{1/4}}{1-(R_1R_2)^{1/2}} \tag{2.21}$$

The parameters conceptually described in this section, such as FSR, Q factor, or Finesse, are used throughout the thesis to characterize our laser.

2.1.2 Simulation

An optical resonator is referred to as a stable resonator if it allows a continuous feedback of the light after an infinite number of round-trips. The stability criterion of an optical resonator depends on the geometry of the resonator. The radius of curvature of the mirrors and the optical distance between them are the geometrical parameters used to describe the stability of an optical resonator. We note once more that the optical length is given by the product of the refractive index of the medium and the spacing between the mirrors ($L = nL_0$).

The geometric parameter of the mirrors of an optical resonator is characterized by a g-parameter, defined as:

$$g_j = 1 - \frac{L}{R_j}, \quad j = 1,2 \tag{2.22}$$

R_j refers to the radius of curvature of the mirrors. The condition necessary for a stable resonator is then expressed as:

$$0 < g_1g_2 < 1 \tag{2.23}$$

A graphical representation in figure 2.3 depicting the stability condition stated in equation 2.23,

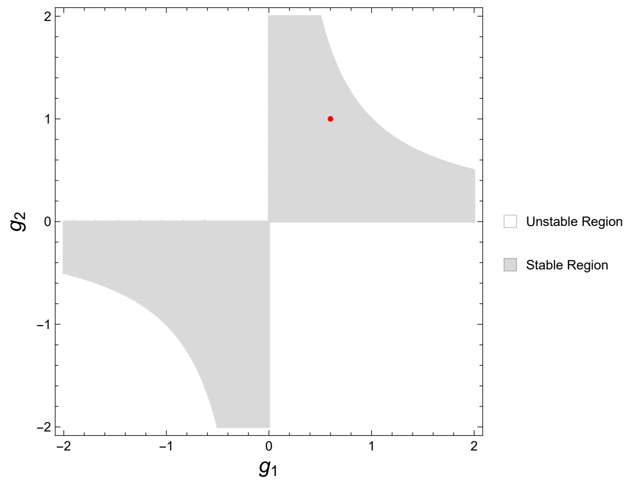

Figure 2.3: Stability diagram of a two-mirror optical resonator. The red dot corresponds to the location of our optical resonator, for $R_1 = 100 \ cm$ and $L_0 = 25 \ cm$.

is produced in Mathematica, showing with a dot the location of our resonator in terms of stability. The shaded regions represent regions of stable resonators, and any optical resonators that fall out of these regions are unstable. Table 2.1 shows different geometrical parameters we have considered for a hemispherical laser cavity, along with their respective $g_1 g_2$. The extreme values corresponding to $g_1 g_2 = 0 \ or \ 1$ are associated to optical resonators which are conditionally stable and therefore challenging to implement. An example of such a resonator is the Fabry-Perot resonator mentioned earlier, having a $g_1 g_2 = 1$.

L_0 (cm)	$g_1 g_2$ ($R_1 = 20 \ cm$)	$g_1 g_2$ ($R_1 = 50 \ cm$)	$g_1 g_2$ ($R_1 = 100 \ cm$)
20	0	0.60	0.80
25	-0.25	0.50	0.75
30	-0.50	0.40	0.70
35	-0.75	0.30	1.30

Table 2.1: Different geometrical parameters of the two-mirror resonators

A simulation based on another approach called the ABCD law, is used to determine the geometrical parameters for any two-mirror optical resonator configuration. This simulation is performed with a software called reZonator, which also allowed the determination of the beam size along the cavity. The optical resonator is made of several optical components of various apertures and therefore, an approximation of the the beam size is needed. The ABCD law models a wave as an optical ray and describes an optical system by relating the input and output of the system through a matrix called the ABCD transfer matrix (M_T). More information regarding the ABCD law can be found in references [22, 23, 21].

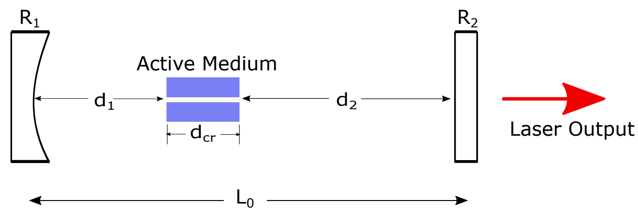

Figure 2.4: Basic components of a Hemispherical Optical Resonator

Each component of the optical resonator system in figure 2.4 can be written in terms of its own ABCD matrix. The product of all the matrices that constitute the optical system is the ABCD transfer matrix. The ABCD matrices of each component are represented as:

$$M_1 = \begin{bmatrix} 1 & 0 \\ -\frac{2}{R_1} & 1 \end{bmatrix}, \; M_2 = \begin{bmatrix} 1 & 0 \\ -\frac{2}{R_2} & 1 \end{bmatrix} \tag{2.24}$$

$$L_1 = \begin{bmatrix} 1 & d_1 \\ 0 & 1 \end{bmatrix}, \; L_2 = \begin{bmatrix} 1 & d_2 \\ 0 & 1 \end{bmatrix} \tag{2.25}$$

$$Cr = \begin{bmatrix} 1 & -\frac{d_{cr}}{nk} \\ 0 & -\frac{1}{k} \end{bmatrix} \tag{2.26}$$

M_1 and M_2 are the ABCD matrices for mirror 1 and 2 with radius of curvature, R_1 and R_2, respectively. L_1 and L_2 represent the free space ABCD matrices. Finally, Cr is the ABCD matrix of the active medium, with an index of refraction n. The optical distance of the active medium is then $d = nd_{cr}$. Note that the k parameter in Cr is the beam expansion factor given by $\cos\phi \cos\theta$, where ϕ and θ are the angle of incidence and refraction, respectively. Both angles are taken to be unity in this case. The ABCD transfer matrix is then written as follows:

$$M_T = \begin{bmatrix} A & B \\ C & D \end{bmatrix} = M_1 \cdot L_1 \cdot Cr \cdot L_2 \cdot M_2 \cdot L_2 \cdot Cr \cdot L_1 \tag{2.27}$$

Using the ABCD transfer matrix, the condition for a stable resonator is established as:

$$-1 \leq \frac{A+D}{2} \leq 1 \tag{2.28}$$

The stability parameter $\frac{A+D}{2}$ is plotted in figure 2.5 as a function of different radii of curvature for the high reflector (R_1). The figure shows that for longer cavity lengths, using a mirror with

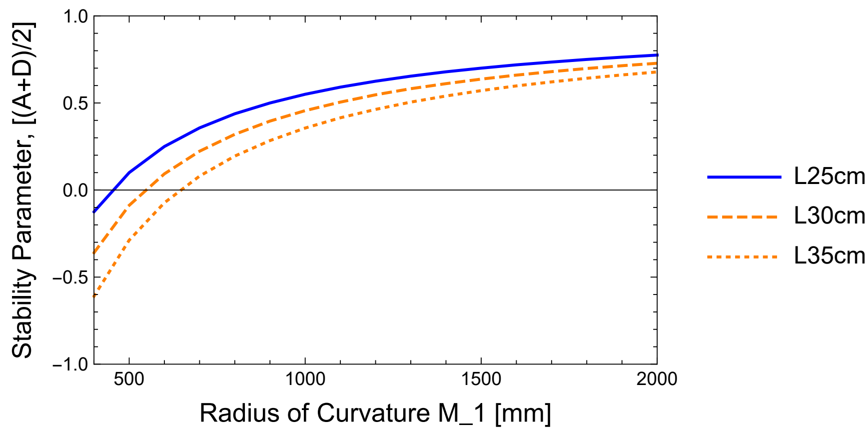

Figure 2.5: Stability map as a function of radius of curvature. The solid curve corresponds to $L = 25$ cm, the dotted curve is for $L = 30$ cm, and the dashed curve is for $L = 35$ cm.

a large radius of curvature improves the stability of the resonator. There is therefore a range of acceptable radii of curvature and spacing between the mirrors that lead to a stable optical resonator configuration. On the other hand, to obtain a smaller beam size, mirrors with shorter radii of curvature are needed, as seen in figure 2.6, which shows a simulation of the variation of the beam size along the cavity for radii of curvature $R = 50$ cm and $R = 100$ cm at either 1064 nm and

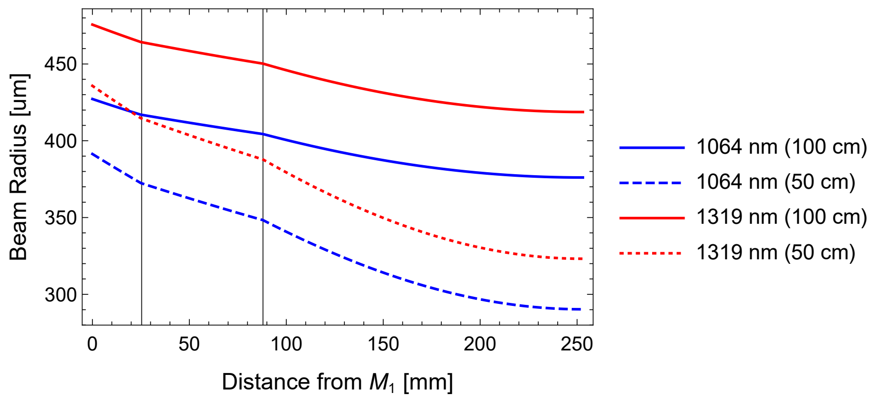

Figure 2.6: Variation of the beam size along the optical cavity for both 1064 *nm* and 1319 *nm*.

1319 *nm*.

2.1.3 Design

Figure 2.7 shows a sketch of our resonator design with its geometrical parameters. The resonator consists of a high reflective spherical mirror, also called high reflector (HR), with a radius of curvature of $R_1 = 100$ *cm*, a partially reflective planar mirror which is the output coupler (OC), and an Nd:YAG gain module which provides the active medium. The index of refraction of the Nd:YAG is 1.8. Between the Nd:YAG and the mirrors, the index of refraction is taken to be unity, such that the optical length of the resonator is $L = nL_0 \approx 30.64$ *cm*.

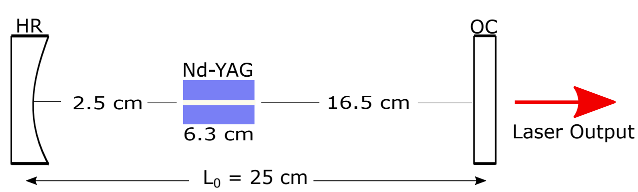

Figure 2.7: Optical cavity design implemented in the experimental set-up

As seen in figure 2.8, the laser cavity designs are identical for both pump lasers, with the exception that the mirrors for the 1064 nm pump laser are suitably coated for radiation with a 1064 nm wavelength, and the mirrors for the 1319 nm pump laser are designed for 1319 nm wavelength. Coating the mirrors at the desired wavelength provides a filtering system for unwanted radiation.

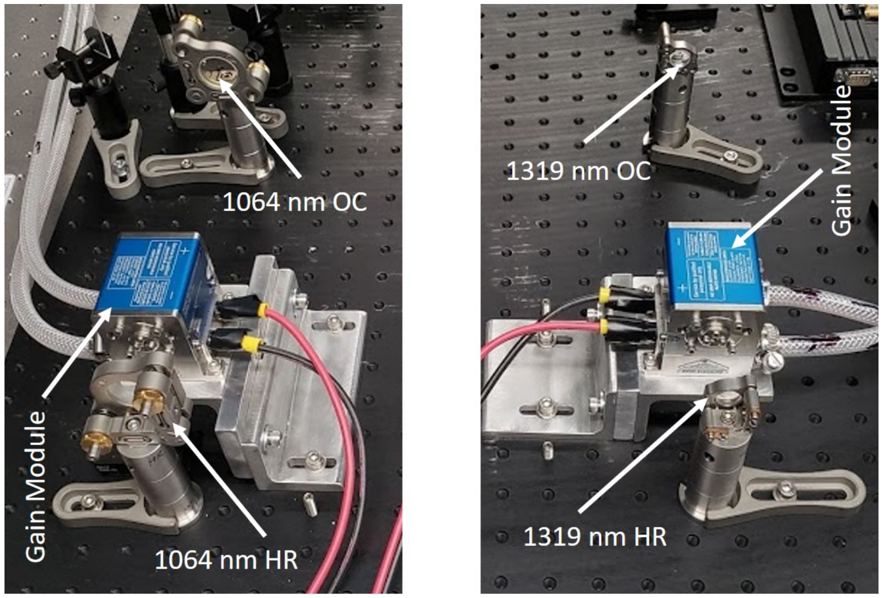

Figure 2.8: Optical cavity set-up for 1064 nm (left) and 1319 nm (right)

Applying a coating layer on the mirrors is particularly important when using a YAG laser. As it is discussed in subsequent chapters, YAG lasers have several emission lines and coating helps to select the desired wavelength. A list of some important parameters of the mirrors is recorded in table 2.2.

Wavelength (nm)	1064	1319
HR Radius of Curvature (cm)	100	100
OC Radius of Curvature (cm)	Planar	Planar
HR Reflectivity (%)	99.80	99.70
OC Reflectivity (%)	90 $\pm$2	97 $\pm$2

Table 2.2: Resonators mirror' parameters for 1064 nm and 1319 nm pump lasers

From the concepts illustrated in section 2.1.1, the estimated FSR of our optical resonator is 490 MHz. Using the parameters listed in table 2.2, the finesse of the cavities are 58.52 and 187.8 for 1064 nm and 1319 nm resonators, respectively. It is also noted from table 2.1 that the cavity losses induced by the HR and OC mirrors are 0.2 %, and 0.3 % for the HR coated at 1064 nm and 1319 nm, respectively. The losses from the OC are 10 % and 3 % for the OC coated at 1064 nm and 1319 nm, respectively.

2.2 Nd:YAG Gain Medium

Any optical resonator experiences losses. These losses could be caused by some or all of the following: the scattering of the medium, the diffraction of the confined beam, or the finite reflection of the mirrors etc. The resonator loss coefficient α is then expressed as [23]

$$\begin{aligned} \alpha &= \alpha_s + \alpha_m \\ &= \alpha_s + \frac{1}{2L_0} \ln\left(\frac{1}{R_1 R_2}\right) \end{aligned} \tag{2.29}$$

where α_m is the loss due to the mirrors, and α_s is the loss caused by scattering and diffraction.

The role of the gain medium is to counter balance those losses by light amplification. For the purposes of our experiment, we have used Neodymium Yttrium Aluminum Garnet (Nd:YAG) as the gain medium, which is essentially a Yttrium Aluminum Garnet (YAG) crystal doped with rare earth Neodymium (Nd) atoms. The Nd:YAG laser is therefore a solid-state laser because it utilizes a solid material as the gain medium.

Figure 2.9 illustrates some possible energy transitions capable of producing a YAG laser [24]. The transitions of interest are represented with solid arrows. The Nd:YAG gain medium is optically pumped by a semiconductor laser at a pumping wavelength of 808 nm, causing the generation of the emission lines seen in figure 2.9. The atoms transition from the ground state energy level $^4I_{9/2}$ to the upper state, $^4F_{5/2}$. Several emission lines (denoted by their respective spectroscopy notations) are produced but the resonators' mirrors are coated to pick up the laser transitions that end at $^4I_{11/2}$ and $^4I_{13/2}$ for the 1064 nm and 1319 nm emitted wavelengths, respectively. We note that for YAG lasers, 1064 nm is the most dominant laser transition ($^4I_{3/2} \rightarrow {}^4I_{11/2}$). The remainder of this section is focused on describing the four-level system of the Nd-YAG laser and understanding how the gain is provided using such a gain medium, in order to produce a laser.

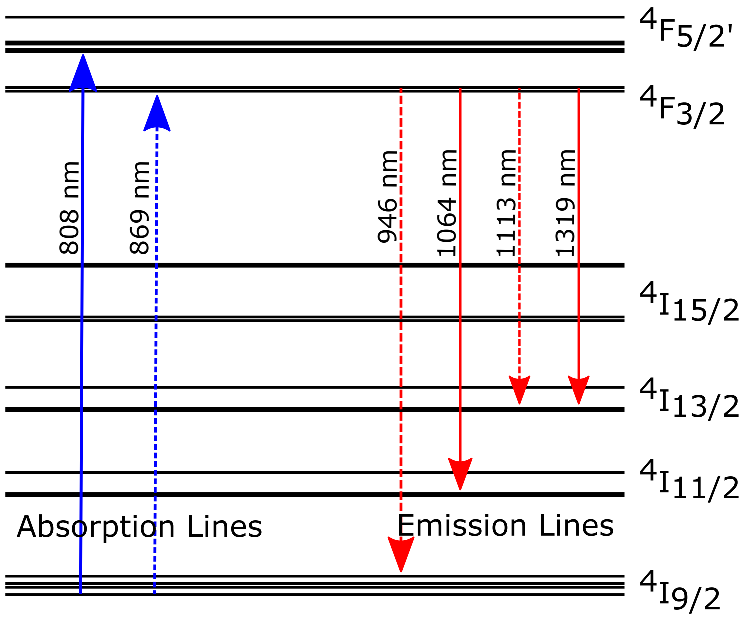

Figure 2.9: Energy-level diagram of an Nd:YAG laser. The solid arrows represent the radiation being used in this experiment. Optical pumping is performed with a laser diode with a center wavelength around 808 nm, and the emission lines considered are for 1064 nm and 1319 nm.

A system of atoms within a material at thermal equilibrium tends to stay on the lowest energy level or ground state of the system. However, a laser is only feasible if there are more atoms on the upper energy level compared to the ground state. Such an unorthodox system is referred to as population inversion. Population inversion is accomplished via optical pumping, a technique in which light is radiated into a system, causing the atoms of the material to absorb photons and inducing a transition to the upper energy state.

The sketch in figure 2.10 perfectly illustrates the processes occurring during optical pumping of a four-level system, denoted as $|g\rangle$, $|1\rangle$, $|2\rangle$, and $|3\rangle$, for the ground, first, second, and third energy level, respectively. In stage 1, the atoms within the system are subjected to a particular radiation of a light field of energy E_{photon}. The photons are observed and in stage 2, the following transition, $|g\rangle \rightarrow |3\rangle$, occurs if the energy of E_{photon} is approximately equal to the energy difference between the states $|g\rangle$ and $|3\rangle$. In a two-level system, the opposite transition immediately

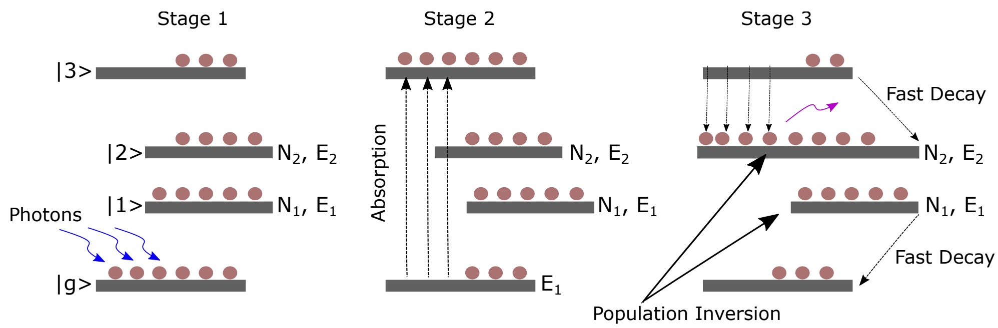

Figure 2.10: Population inversion of a four energy-level system

occurs. However, for a four level system, the transition $|3\rangle \rightarrow |g\rangle$ is interrupted by the state $|2\rangle$, known as a meta-stable state. Due to a fast decay, the atoms fall onto the E_2 energy level as seen in stage 3. Spontaneous and stimulated emissions cause the atoms to decay onto the energy level E_1, therefore creating a population inversion between these two states, with a release of energy that is proportional to $E_2 - E_1$. The stimulated emission establishes a gain on the transition $|2\rangle \rightarrow |1\rangle$. Eventually, the atoms fall back onto $|g\rangle$ until optical pumping is applied again.

In summary, there are three processes occurring during optical pumping of a system [23] . Absorption, spontaneous emission and stimulated emission, such that,

$$Total\ \ rate\ \ of\ \ absorption = Total\ \ rate\ \ of\ \ emission \tag{2.30}$$

where the total rate of emission is the sum of spontaneous emission and stimulated emission.

Equation 2.30 can also be expressed in terms of Einstein A and B coefficients, as:

$$N_1 B_{12} \rho(h\nu_{12}) = A_{21} N_2 + N_2 B_{21} \rho(h\nu_{21}) \tag{2.31}$$

B_{12} is the Einstein coefficient for the absorption process.

B_{21} is the Einstein coefficient for the stimulated emission process.

A_{21} is the Einstein coefficient for the spontaneous emission process.

N_1 and N_2 are the number densities of atom in states $|1\rangle$ and $|2\rangle$, respectively.

$\rho(h\nu)$ represents the energy density of the pump light.

The photons produced by stimulated emission are called gain. This gain is then amplified by means of a feedback system created by the mirrors. Gain amplification is illustrated in figure 2.11. Considering an initial beam of light close to the center of the cavity (position 1) enters the gain medium and experiences a photon loss due to scattering of photons caused by imperfection of the surface of the gain medium (position 2). In Position 3, the light beam gains energy because of stimulated emission occurring inside the medium. As it escapes out of the gain medium, there is

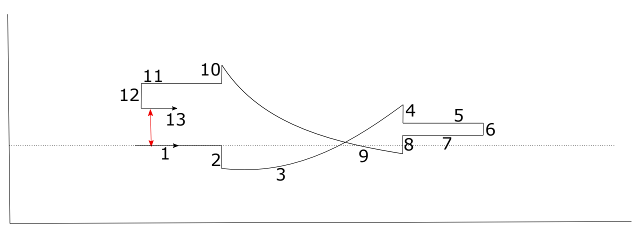

Figure 2.11: Gain along an optical cavity

a slight loss (position 4) due to a partial reflection once again. The beam then propagates towards the output coupler (OC) in position 5, and because the OC is only partially reflective, there would be losses as seen in position 6. As the light beam bounces off the OC, the same processes occur for positions 7, 8, and 10 but in the opposite direction. In position 11, the beam exits the gain medium with a higher intensity but loses some of the energy bouncing off the high reflective mirrors, because some portion of the light is not being reflected due to absorption. However, after one-round as seen in position 13, the light beam has gained more energy compared to its initial energy and the resonator is acting as a laser.

The gain coefficient, $\gamma(\nu)$, of lasers is defined by the following equation:

$$\begin{aligned}\gamma(\nu) &= \left[A_{21}\frac{\lambda^2}{8\pi n^2}g(\nu)\right]\left[N_2 - \frac{B_{12}}{B_{21}}N_1\right] \\ &= \sigma_{21} \times N^*\end{aligned} \tag{2.32}$$

where, λ is the pump wavelength. $g(\nu)$ is the line shape function, describing the light-matter interaction. σ_{21} is the optical gain cross section of the laser transition. N^* is the population inversion density. In tables 2.3 and 2.4, laser parameters and the YAG rod characteristics are given.

Wavelength (nm)	1064	1319
Transition	$({}^4I_{3/2} \rightarrow {}^4I_{11/2})$	$({}^4I_{3/2} \rightarrow {}^4I_{13/2})$
σ_{21} (cm^2)	3.7×10^-19	9.5×10^-20

Table 2.3: Nd:YAG laser parameters for 1064 nm and 1319 nm transitions

Nd:YAG Material Parameters	Value
Density of Nd Atoms	1.38×10^{20} (cm^{-3})
Index of Refraction	1.82
Scattering losses	0.002 (cm^{-1})
Fluorescence Lifetime of ${}^4I_{3/2}$	233 μs

Table 2.4: Nd:YAG Material Parameters

2.3 Laser System Assembly

Laser system assembly involves installation of the gain module, setup of the chillers, connection of the chillers to the gain module, and configuration of the eDrive controller for the gain module. Installation of the gain module on the optical breadboard requires particular care as you must align the optical cavity precisely in order to ensure stability. The eDrive controller and chillers are configured according to manufacturer guidelines to ensure optimum performance.

2.3.1 Chiller for Laser Cooling

Before any operation of the gain module, chillers should be connected to the module and turned on to provide a water cooling system to control the temperature of the gain module. Hoses are connected from the gain module to the back panel of a chiller, which is composed of a chiller reservoir and filter. Figure 2.12 shows a picture of the front and back of the chiller. The front panel of the chiller allows one to change the temperature and pressure settings. The coolant used is a mixture of 10 % Optishield Plus$_{TM}$ and 90 % distilled water. The pump module final test sheet performed by Northrop Grummann specifies that the optimum operating temperature of the modules is 28° Celsius. The chillers are therefore set to run at that temperature.

Figure 2.12: Chiller's front and back panels

2.3.2 Installation of Gain Module

As it has been mentioned previously, the active medium is provided by the yttrium aluminum garnet (YAG) crystal doped with neodymium (Nd) atoms, producing a Nd:YAG gain medium. The crystal is enclosed in a module made by Northrop Grumman-Cutting Edge Optronics. Operating limits of Nd:YAG gain module in a quasi-continuous wave (QCW) operating mode are listed in table 2.5. The table shows that when triggering pulses, the repetition rate of the pulses should be set as to not exceed 7.9 % duty cycle.

Parameters	QCW Operating Limits
Current (A)	≤ 147
Voltage (V)	≤ 56.7
Pulse Width (μs)	157.5
Duty Cycle (%)	≤ 7.9

Table 2.5: Nd:YAG gain module operating limits

Figure 2.13 is a picture of the Nd:YAG gain module, which is the same for both 1064 nm and 1319 nm resonators. The gain modules are mounted on a XYZ adjustable holders with an adjustment of couple of centimeters.

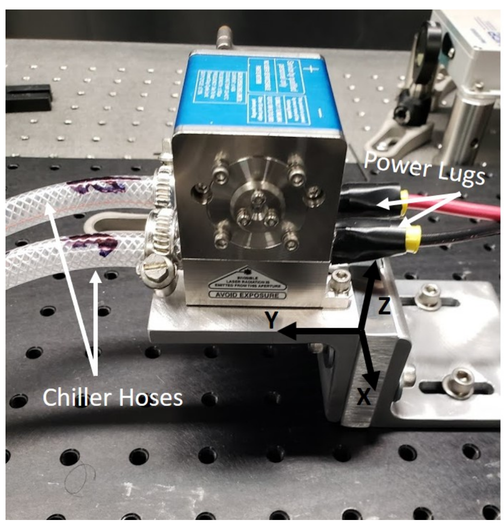

Figure 2.13: Gain Module for either 1064 nm or 1319 nm pump lasers.

A general design setup of the gain module connections in figure 2.14 shows that the gain module is controlled by an eDrive. The eDrive, as mentioned in table 2.5, can deliver a maximum current of 147 A to generate current pulses used to pump the gain medium. The connections necessary to power up the laser gain module are also shown. The laser gain module is connected to a laser system controller (eDrive). The eDrive can be used for all diode-pumped solid-state (DPSS) laser parameters including the diode drive current, the Q-switch, and system interlocks. It is capable of driving diodes in either continuous wave (CW) or quasi-continuous wave (QCW) operating mode. The eDrive controller and power supply for 1064 nm lasers are shown in figure 2.15. Identical units are implemented for 1319 nm. A similar system is used for the 1319nm laser.

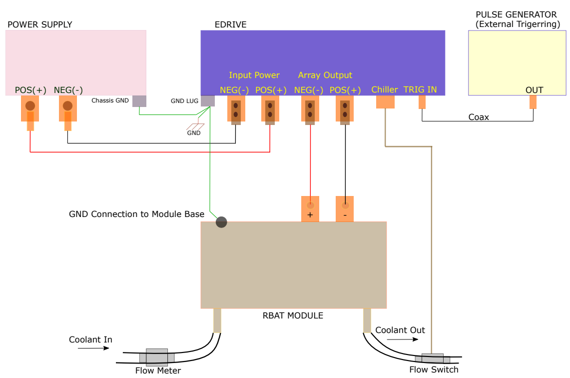

Figure 2.14: Basic illustration of the gain module connections

Figure 2.15: eDrive controller (top) and power supply (bottom) for 1064 nm laser

Once the connections are performed, the chillers are turned on, and are left to run until they have stabilized to the set temperature (28° Celcius in this case). The laser gain module is then powered up by turning on the power supply and the eDrive. The internal trigger of the eDrive is used to send information to the gain module, such as the repetition rate, the pulse width, and the current at which pumping should be performed. A duty cycle limit is also set. Only once all the parameters are set, and the connections are checked, the eDrive is set to emission, which produces the optical pumping mechanism described in the previous section. The fluorescence at 808 nm is then seen using an infrared (IR) card, as shown in figure 2.16. The module is later on inserted into the cavities to generate a feedback system as a mean to increase the laser gain. Figure 2.17 shows the set-up of both cavities mounted on a 24×36 in optical breadboard. In figure 2.21, the 1319 nm cavity is shown to be lasing. In the next chapter, laser characterization is performed. The alignment of the optical cavity is described in the next section.

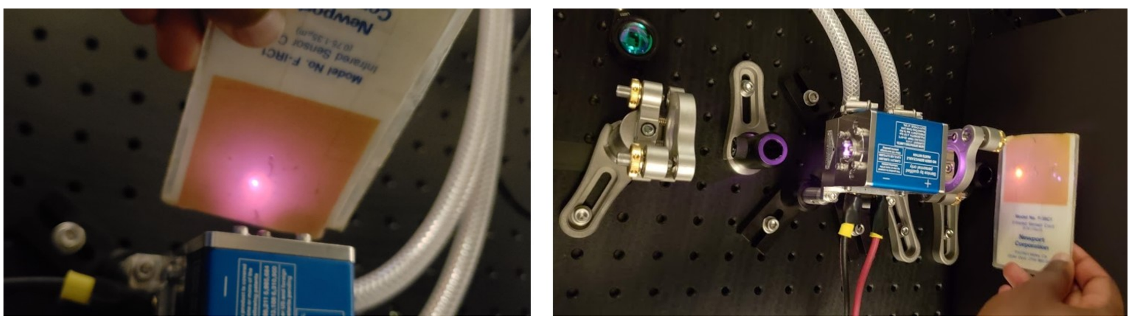

Figure 2.16: 808 nm fluorescence due to optical pumping (left) & gain module inserted into the 1064 nm optical cavity (right)

2.3.3 Optical Cavity Alignment

The 1064 nm and 1319 nm laser resonators are composed of one-inch and half-inch mirrors, respectively. The mirrors are mounted on three-inch post holders with kinematic mounts. To align the resonator [25] such that the mirrors are parallel to each other, an external collimated diode laser, with a center wavelength of 1064 nm, is used. A sketch of the alignment is presented in figure 2.18. An indication of cavity misalignment is the presence of multiple back reflections as illustrated in figure 2.19. To ensure that the mirrors are aligned, the back reflections are made to

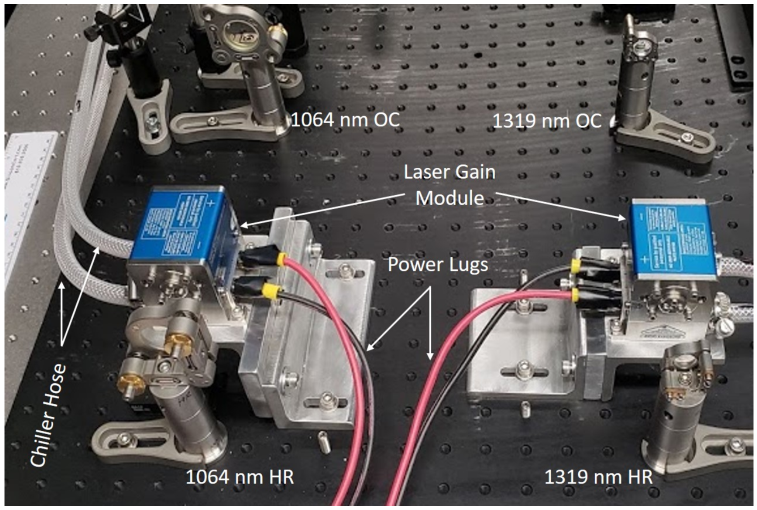

Figure 2.17: Set-up of both optical resonators, 1064 nm (left) and 1319 nm (right)

overlap with the main beam by using the adjustable knobs on the mirror' mounts.

The laser gain module is inserted into the cavity, after ensuring that the mirrors are properly aligned. As mentioned earlier, the gain modules for both 1064 nm and 1319 nm lasers are mounted on XYZ adjustable holders to facilitate the coupling of the laser diode into the Nd:YAG crystal. It is important to note that the placement of the module relative to the alignment beam is

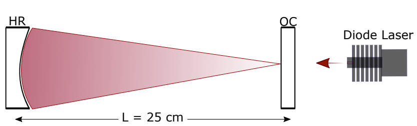

Figure 2.18: Resonator alignment setup

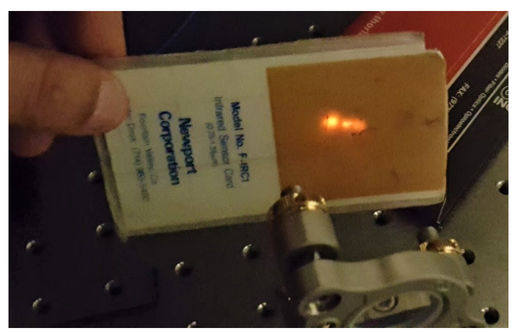

Figure 2.19: Back reflections caused by the 1064 nm cavity misalignment

crucial, because the end of the rod has a 2° angle that could cause the beam to be clipped. For instance, if we consider the case of the 1319 nm resonator which is made of mirrors with 1/2 inch diameters, the beam exiting the rod towards the the output coupler will exit at a 4° angle. Because the distance between the end of the rod and the mirror is about 16.5 cm, the beam will hit the mirror, about 1.15 cm away from the center of the mirrors. Since the mirror diameter is 1.27 cm, one therefore acknowledges that a slight misalignment will cause the beam to be clipped and consequently, produce an unstable resonator.

CHAPTER 3

LASER CHARACTERIZATION

The goal of this chapter is to evaluate the performance of the lasers by analyzing the optical output of the laser beam by using a power meter, a photodiode, and a beam profiler. Measurements such as power scaling, power stability and beam characterization are performed.

3.1 Power Scaling

To achieve power scaling [26] is achieved with the following requirements: the increase of pump power is done by changing only one variable, and repeated measurements are feasible and lead to the same outcome. One major concern of power scaling is the thermal lens effect of the laser rod crystal. Thermal lens effect is caused by heating of the laser rod, inducing aberrations on the beam. At extremely high power, thermal lensing becomes significant and can affect the performance of the laser. Therefore, power scaling is performed below the limit of thermal lensing.

The pump power is increased by increasing the input current sent to the laser gain medium, ranging from 40-80 Amperes. With a pulse duration (width) of 150 μs and a beam diameter of about 1 mm, different repetition rates (100 Hz, 300 Hz, and 500 Hz) are considered during power scaling measurements. A trend-line similar to a linear fit is observed between pump power and optical output power, as shown on the plots of figure 3.1 and 3.2. In tables 3.1 and 3.2, a list of measured and calculated parameters are presented, for 1064 nm and 1319 nm, respectively.

It is noted that at lower repetition rates, the two lasers output a similar average power but the difference in output power becomes bigger as the repetition rate increases. For instance, at

100 Hz with a current of 80 Amps, the percentage difference of their respective maximum output power is only 2.23 %, while at 500 Hz with the same current, the percentage difference is 29%. The high average output power obtained for 1064 nm could be due to both the fact that the 1064 nm transition line has a stronger gain compared to the 1319 nm, and also that the reflectivity of the OC for 1064 is only 90 % compared to 97% for 1319 nm. The 1319 nm laser needs a high HR particularly due to its low gain.

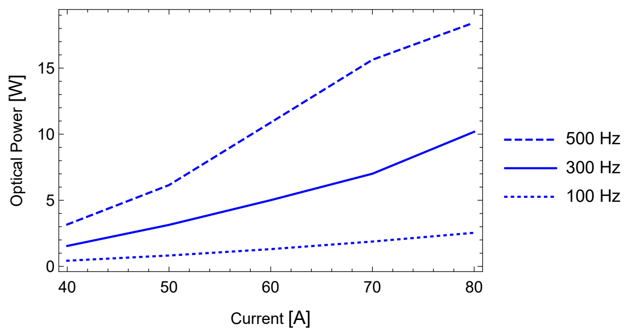

Figure 3.1: Power scaling of 1064 nm pump laser

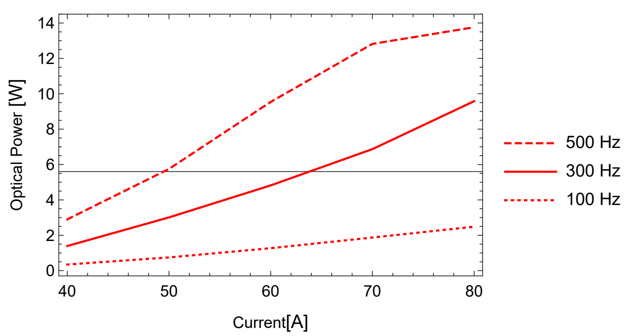

Figure 3.2: Power scaling of 1319 nm pump laser

The power scaling plots also show noticeable inflection points. At 500 Hz for example, the curves for for 1064 nm and 1319 nm both change at a current of approximately 50 Amps and 70 Amps. As it is described later, the YAG lasers are found to produce the right input pump pulse at about 50 Amps. A slope efficiency is then calculated by recording the average power output above 50 Amps. A plot of optical power versus current for the 1319 nm is shown in figure 3.3. A

Parameters	100 Hz	300 Hz	500 Hz
Power @80 Amps (W)	2.542 (W)	10.18	18.44
Power @40 Amps (W)	0.429	1.547	3.17
RMS	1.58	6.17	12.25
Standard Deviation	0.84	3.37	6.35
Least Squared Fit	-1.77+0.053x	-7.30+0.211x	-13.16+0.40x
R-Squared	0.99	0.98	0.9915

Table 3.1: Fitting Parameters for 1064 nm

Parameters	100 Hz	300 Hz	500 Hz
Power @80 Amps (W)	2.49	9.58	13.76
Power @40 Amps (W)	0.347	1.394	2.9
RMS	1.55	5.89	9.86
Standard Deviation	0.86	3.22	4.62
Least Squared Fit	-1.90+0.054x	-7.00+0.20x	-8.32+0.29x
R-Squared	0.99	0.99	0.97

Table 3.2: Fitting Parameters for 1319 nm

linear fit is performed on the data and the obtained least squared fit is listed in table 3.3. Using the fit equation, the threshold pump power is determined to be approximately 34 Amps. This value is obtained by looking at the point where the linear fit crosses the current axis (i.e x axis).

Parameters	300 Hz
Standard Deviation	0.832355
Least Squared Fit	-6.08+0.18x
R-Squared	0.9999

Table 3.3: Fitting Parameters for 1319 nm & slope efficiency

From the measured maximum average optical output power, values such as pulse energy and peak power are calculated for different repetition rates, using the following set of equations:

$$Pulse\ \ Energy(J) = \frac{Average\ \ Power(W)}{Repetition\ \ Rate(Hz)} \tag{3.1}$$

$$Peak\ \ Power(W) = \frac{Pulse\ \ Energy(J)}{Pulse\ \ duration(s)} \tag{3.2}$$

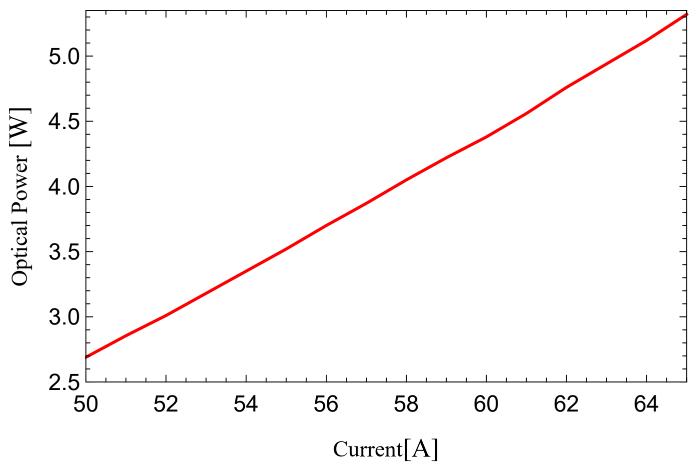

Figure 3.3: 1319 nm pump laser power scaling above 50 Amps at 300 Hz

$$Linear\ \ Power\ \ Density(\frac{W}{cm}) = \frac{2 \times (Average\ \ Power)}{(1/e^2)Beam\ \ Diameter} \tag{3.3}$$

$$Energy\ \ Density(\frac{J}{cm^2}) = \frac{2 \times (Pulse\ \ Energy)}{\pi(\frac{(1/e^2)\ \ (Beam\ \ Diameter)}{2})^2} \tag{3.4}$$

Parameters	**100 Hz**	**300 Hz**	**500 Hz**
Pulse Energy (J)	0.025	0.034	0.037
Peak Power (W)	169.47	226.22	245.88
Linear Power Density (W/cm)	1382.19	553.41	1002.40
Energy Density (J/cm^2)	47.83	63.84	69.39

Table 3.4: Energies values for 1064 nm

Parameters	**100 Hz**	**300 Hz**	**500 Hz**
Pulse Energy (J)	0.025	0.032	0.028
Peak Power (W)	165.733	212.89	183.47
Linear Power Density (W/cm)	135.15	520.79	748.03
Energy Density (J/cm^2)	46.77	60.04	51.78

Table 3.5: Energies Values for 1319 nm

Pulse energy, peak power, linear power density and energy density are found to increase linearly with the repetition rate as shown in tables 3.4 and 3.5. The eventual outcome of building these pump lasers is to perform sum-frequency generation (SFG) to obtain a Na laser system with an optical power of 2-5 W. However, the power scaling plots in 3.1 and 3.2 show that repetition rates below 300 Hz do not produce sufficient power output for SFG. In the case of the 1319 nm pump laser for example, a mininum power of 5 Watts is necessary for SFG and at 300 Hz, a 65 Amps pump current is needed to produce such output power.

3.2 Power Stability

An analysis of laser power stability is a convenient method of determining the consistency of measurements performed [27]. For instance, laser applications (i.e. atomic spectroscopy application) that require precise output power level, may produce fewer usable data points if performed with an unstable laser. It is therefore essential to understand how the laser system behaves before any operation.

Basic requirements for laser stability to be considered are: 1) the laser gain medium should be warmed-up before any use. 2) test set-up should be repeatable, such as environmental, cooling system, etc. To demonstrate how significantly the first requirement affects the stability outcome of the laser, a power stability measurement is recorded, right after the laser is turned on for the 1319 nm (figure 3.4), and about twenty-minutes of laser emission for 1064 nm laser (figure 3.5). Both figures show a slow increase of optical power. However, the slope is less prominent in figure 3.5 because the laser had started to reach its equilibrium state. Fluctuations in figure 3.4 are calculated to be about 0.0349364 in terms of standard deviation (STD). In figure 3.5, the STD is 0.010524.

The case made here is not to compare the stability between both lasers, but rather to show that, either pump lasers require an equilibrium system before being put to use. From figure 3.4, it is possible to determine that the lasers need to warm-up for at least thirty to sixty minutes.

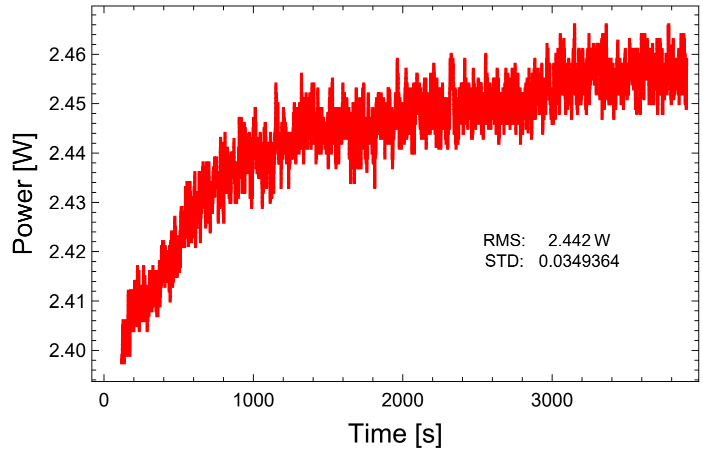

Figure 3.4: 1319 nm pump laser demonstrating power instability

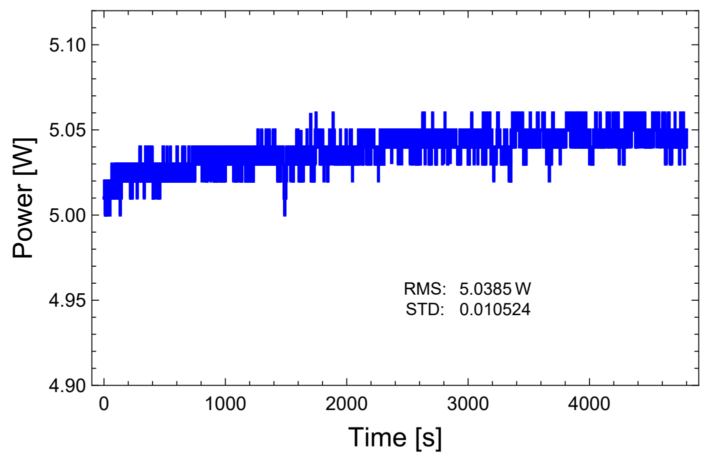

Figure 3.5: 1064 nm pump laser power stability

A long-term power stability measurement is then reproduced with the 1319 nm pump laser, with a warm-up time of about forty-minutes, and a data collection time of one to two hours.

The requirements stated earlier are followed as such - The chiller is first turned on approximately twenty-minutes before the gain module is powered-up. This is to ensure the gain medium has reached an equilibrium temperature. Pulse duration, repetition rate, and input pulse current are set on the eDrive, with values of 150 μs, 500 Hz, and 50 Amps, respectively.

Once laser emission is on, the gain module is also let to run for about an hour before the recording of data. After the one hour elapsed time, the optical average power is recorded using the Vega Ophir power meter, P/N: 7Z01560. The Vega ophir power meter is connected to a thermal sensor that allows reading of high power. Figure 3.6 shows the stability plot obtained for the 1319 nm pump laser. An improvement in stability is obtained with a fluctuation of only 0.007479 in STD, which is an order of magnitude lower compared to figure 3.4.

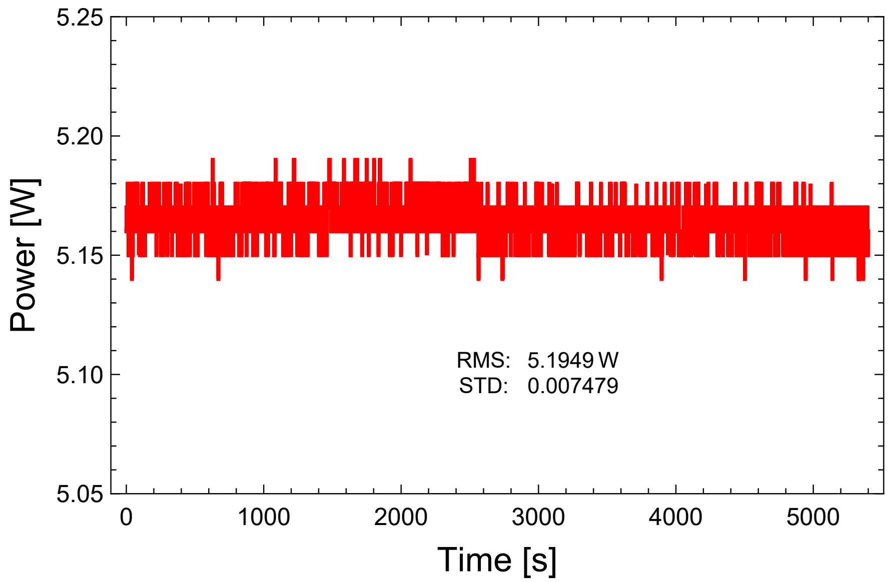

Figure 3.6: 1319 nm pump laser power stability

It is essential to note that even though there is an improvement in fluctuation between figures 3.4 and 3.6, the system still shows some variation in power after warm-up. There are several other types of noises that can contribute to fluctuation in laser stability, and that have not been addressed. Sources of noise could range from random errors caused by the detector being used, inducing thermal noise in the data, to background radiation noise. The topic of noise is not being discussed in this thesis, but more information on laser noise is found in reference [28]. As a conclusion, laser systems show fluctuation of power or light intensity and it is therefore necessary to study the performance of a particular laser before utilization.

3.3 Beam Characterization

In chapter one, it is shown that by using the concept of ray tracing, important information of the beam propagating within an optical resonator are obtained. Nevertheless, there is a drawback because electromagnetic waves have both an amplitude and a phase, and therefore, missing pieces of information of the beam are unraveled by looking at the profile of the beam. In this section, the beam profile [29] of the laser beam is presented as well as the characterization of output pulses generated by the lasers.

3.3.1 Beam Profile

A laser beam propagating along the optical axis of the system generates a fundamental mode known as the Gaussian beam. However, any deviation from this optical axis due to misalignment of the laser cavity, produces higher order modes (HOM) called transverse modes. These transverse modes are therefore different from the intrinsic longitudinal modes of any optical resonator, in the sense that the longitudinal modes are decided by the shape of radii of curvature of the mirrors forming the cavity and are therefore always present. Transverse modes on the other hand, are eliminated by a perfect alignment of these mirrors.

By describing an optical beam in terms of its transverse electric and magnetic fields (TEM), The fundamental mode (Gaussian beam) is generally expressed as TEM_{00} and so, the transverse modes are written as TEM_{0n}, where n represents the number of transverse modes. Mathematically, a confined Gaussian beam in a homogeneous medium is represented as [23, 28]:

$$\begin{aligned}\frac{E(x,y,z)}{E_0} &= \left(\frac{\omega_0}{\omega(z)} exp\left[-\frac{r^2}{\omega^2(z)}\right]\right) \\ &\times exp\left(-j\left[kz - tan^{-1}\left(\frac{z}{z_0}\right)\right]\right) \\ &\times exp\left[-j\frac{kr^2}{2R(z)}\right]\end{aligned} \tag{3.5}$$

where $\omega(z)$, $R(z)$, and z_0 are given by,

$$\omega^2(z) = {\omega_0}^2(z)\left[1 + \left(\frac{\lambda_0 z}{\pi n {\omega_0}^2}\right)^2\right] = {\omega_0}^2\left[1 + \left(\frac{z}{z_0}\right)\right] \tag{3.6}$$

$$R(z) = z\left[1 + \left(\frac{\pi n {\omega_0}^2}{\lambda_0 z}\right)^2\right] = z\left[\left(\frac{z_0}{z}\right)\right] \tag{3.7}$$

$$z_0 = \frac{\pi n {\omega_0}^2}{\lambda_0} \tag{3.8}$$

The first term in equation 3.5 is the amplitude factor of the beam describing the spreading of the beam. The second term is related to the longitudinal phase factor symbolizing the shift from plane wave to spherical waves. Finally, the last term in 3.5 is the radial phase factor which shows how the phase of the beam changes in the radial direction.

Note: The variables in equations 3.6-3.8 are defined as follows-k is the wavenumber, n is the index of refraction, ω_0 is the beam radius or beam waist, λ_0 is the wavelength of the light in free space, z_0 is the Rayleigh range (describing the amount of diffraction spread i the beam), and R(z) is a radius of curvature (i.e. distance from the beam waist), and ω(z) is a spot size function describing changes of the beam with respect to z.

On the other hand the function that represents higher transverse modes ($TEM_{l,m}$) is in the form:

$$
\begin{aligned}
\frac{E(x,y,z)}{E_{l,m}} =& H_l\left[\frac{\sqrt{2}x}{\omega(z)}\right]H_m\left[\frac{\sqrt{2}y}{\omega(z)}\right] \\
&\times\frac{\omega_0}{\omega(z)}exp\left[-\frac{x^2+y^2}{\omega^2(z)}\right] \\
&\times\left[-j\left(kz-(1+l+m)tan^{-1}\left(\frac{z}{z_0}\right)\right)\right] \\
&\times exp\left[-j\frac{kr^2}{2R(z)}\right]
\end{aligned}
\tag{3.9}
$$

where $H_{l,m}$ are Hermite polynomials of order l and m. Even though there are resemblance between equation 3.9 and 3.5, the phase shift in 3.9 now depends on l and m, which changes the frequency oscillation of a laser beam and causes the field distribution to vary. The l value describes this field distribution and tells how many times the field intensity of the light has gone to zero. The divergence of a beam from a Gaussian beam is gauged by the M^2 parameter, which is unity for a Gaussian beam. However, for a beam that carries higher-order modes, the value of M^2 can be much greater than one, depending on the number of modes the beam has. In general, a large M^2 value indicates a large deviation from the Gaussian profile.

The beam profile of the 1064 nm pump laser above the YAG threshold is investigated using the Ophir spiricon beam profiler, LBS-300s-NIR in figure 3.6. However, operating the laser at such high current, and consequently high power, is capable of damaging devices or optics with a low damage threshold.

Fortunately, the Ophir beam profiler comes with the LBS-300s that has a system of two beam splitters (BS) built in to reduce the amount of light imparting the detector. The BS have a 1% reflection per surface, and so with 4 Watts in the initial beam, the first beam splitter would reflect 40 mW such that the second beam splitter will send only 400 uW towards the camera. The rest of

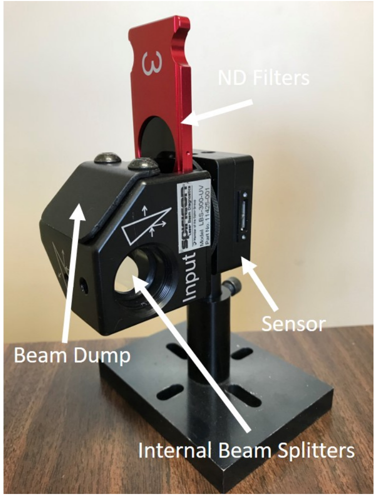

Figure 3.7: Beam profiler

the beam is either transmitted or dumped into the beam dump. Additional filters can be inserted in front of the detector if necessary.

The observed profile of the beam is shown in figure 3.8. The laser does not have a Gaussian distribution but rather, a TEM_{20} field distribution, which means there are several transverse modes in the beam.

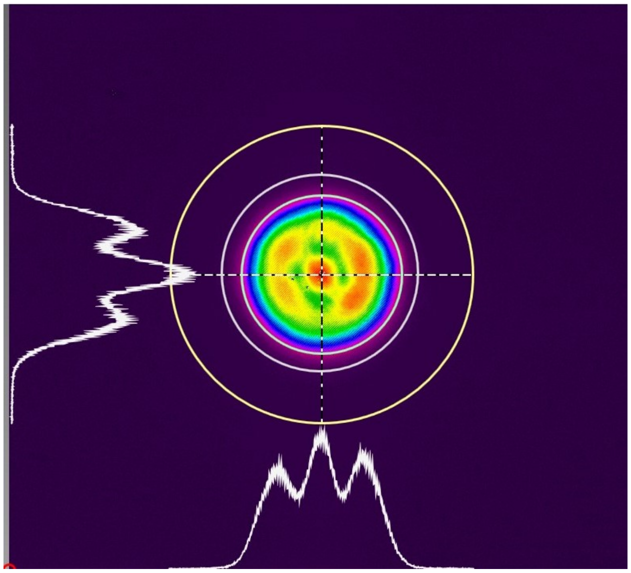

Figure 3.8: 2D intensity distribution of 1064 nm laser

Parameters	Values
Width in X (μm)	4.36 e^{+3}
Width in Y (μm)	2.40 e^{+3}
Average Power Density (cnts)	618.69
Peak (cnts)	4,095

Table 3.6: Fundamental properties of the laser beam

A table of statistical values and fundamental properties describing the beam are listed in table 3.5. The M^2 is found from the waist width and beam divergence from the following relation:

$$\theta = M^2 \times \frac{\lambda}{\pi \omega_0} \tag{3.10}$$

From equation 3.10, a high M^2 indicates a large spot size of the beam.

3.4 Long Pulse Characterization

Pulse characterization is performed by analyzing the shape and pulse width of the laser output, using the Thorlabs DET10A Si biased detector connected to an oscilloscope. The DET10A is a variable gain detector, and pulse width measurements are done with the detector set to a zero dB gain, with a corresponding bandwidth of 1.0 MHz, which corresponds to a response time of 1.0 μs. Pulses at different input currents and at different duty cycles are inspected.

3.4.1 1064 nm Laser Pulses

In the previous section, it is shown that the output of an optical resonator can have transverse modes [30]. The number of transverse modes found in a cavity is closely related to the alignment of the laser cavity, causing the propagation axis of the beam to deviate from the optical axis. Different transverse modes have different intensity distribution and can therefore cause losses in average power. Another consequence of these transverse modes is the appearance of spikes on the laser output pulse. This behavior is clearly seen in figure 3.9.

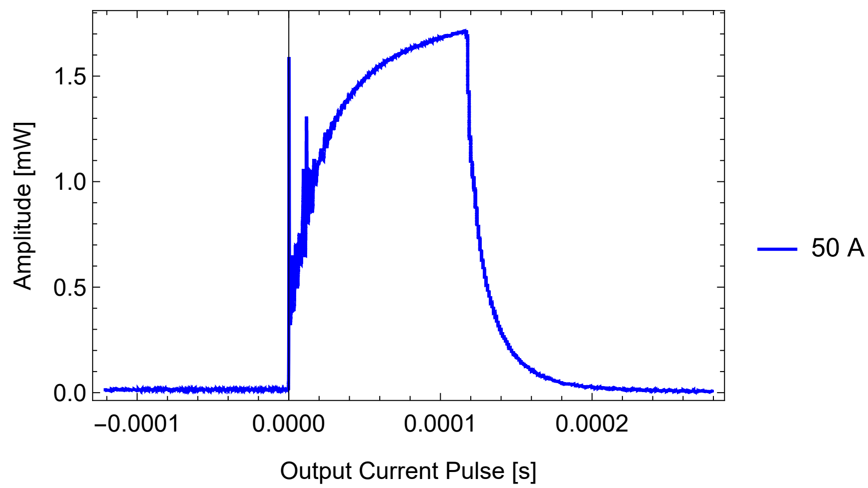

Figure 3.9: Output current pulse of 1064 nm laser

When the laser is set to emission (i.e. pumping source is switched on), there are initially no photons within the cavity until the threshold pump power is achieved. Photons that contribute to the laser are generated once population inversion has reached its threshold value. This explains the slow rise time of the pulse in figure 3.9. On the other hand, the fast decay of the pulse conveys that, as the photon density increases within the cavity, population inversion quickly drops below the threshold causing the lasing to stop. The laser pulse also shows an initial power spike, suggesting that the Nd-YAG laser is capable of storing energy, which could be a cause of a degrade in the laser performance.

Different pulse widths are measured for the 1064 nm laser, using the Thorlabs PDA36A silicon amplifier detector. The PDA36A has a bandwidth ranging from DC-12 MHz, and is capable of detecting wavelengths from 350-1100 nm. The current pulses used to pump the gain medium ranges from 100-300 μs, with a repetition rates of 100 Hz. The current is set above the threshold current. The detector is connected to an oscilloscope that has a 1 MΩ impedance. Matching the impedance of the oscilloscope to the detector with a 50Ω terminator improved the number of spikes observed on the pulses.

However, from figure 3.10, it is determined that shorter pulses are not ideal because there is still a strong presence of spikes by the time population inversion drops below threshold. Nevertheless, there are limitations on the allowed pulse widths, set by the duty cycle ($\leq$7.9 %) of the gain module, and the fluorescence lifetime of the laser, which is 240 μs.

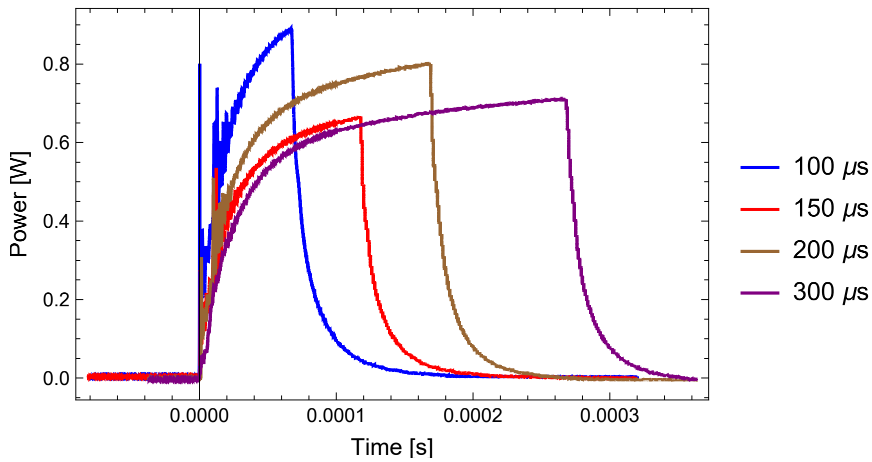

Figure 3.10: 1064 nm laser pulses at different pulse widths

Duty cycle is determined by the product between the current pulse width and the repetition rate. A list is given in table 3.7

Current Pulse Width (μs)	**Duty Cycle (%)**
100	1
150	1.5
200	2
300	3

Table 3.7: Duty Cycle in terms of current pulse widths

It is important to note that though at a repetition rate of 100 Hz, it could have been possible to analyze higher pulse widths, one has to also consider the fluorescence lifetime of the YAG laser. with a lifetime of μs, pumping a QCW laser with a 300 μs pulse width basically turns the laser into a CW, which eventually induces a buildup of heat within the cavity.

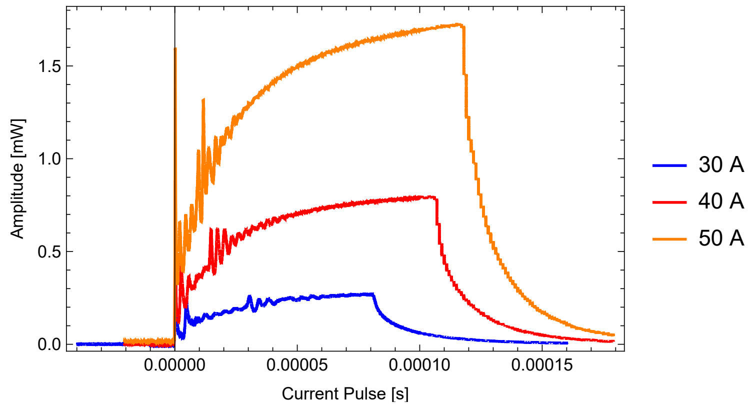

Figure 3.11: 1064 nm laser pulses at different currents

Another characteristic of the pulsed laser that is important to investigate, is the dependence of the pulses on the pump current. Currents at 23 A, 30 A, 40 A, and 50 A are plotted in figure 3.11. All current pulse are given a 150 μs pulse width and a 100 Hz repetition rate. However, the plots show that the lasing starts to occur at about 50 A and below this value, there is not enough pumping energy to produce a laser. This determines the minimum pump current necessary to achieve population inversion.

CHAPTER 4

SHORT-PULSE GENERATION: Q-SWITCHING

A Q-switched laser is capable of producing pulses ranging from micro to nanoseconds [31] by suddenly changing the Q factor of a resonator from a low to a high Q value. As stated in chapter 2, the Q factor determines the quality of the resonator and it is simply defined as the ratio between the resonance frequency of the cavity with the full width half max (FWHM) of that resonance curve. In a low Q resonator, there is no laser oscillation because population inversion does not occur due to a high threshold, and therefore, the gain of the resonator is lower than the cavity losses. A sudden change to a high Q causes any stored energy within the active medium to be released in one single pulse. This is the essence of Q-Switching.

There are two types of Q switching techniques leading to such pulses: active and passive Q-switching [32]. An active QS uses electro-optical switches [23] to reverse the state of the resonator from a low to a high Q, and vice verse. A passive QS on the other hand, operates with a saturable absorber. The main advantage of utilizing an active QS is the control over the timing of switching it provides. In a passive Q-switching, the laser itself is in control of the time of switching.

Other than the saturable absorber and the electro-optic switch, there are several other types of QS devices such as, mechanical QS (i.e. rotating mirrors or shutters) or acousto-optic modulator. Nevertheless, these devices work under the same principle of preventing a laser oscillation until population inversion has reached a maximum. Additional information on these types of devices can be found in [23].

This chapter describes how to produce a Q-switch pulse by means of active Q-Swithching with an electro-optics modulator: a Pockels' cell. Limitations of such a QS are later on presented by comparison with mode-locking, another technique used to obtain short pulses of light.

4.1 Pockels' Cell

Pockels' cells [33] are made with a crystal that exhibits a birefringence behavior when subjected to an electric field (or high voltage), such that the polarization of the light passing through the cell changes according to the index of refraction of the crystal. A general cavity configuration that utilizes a Pockels' cell is shown in figure 4.1. The laser light propagates along the cavity mirrors and the polarization of the light is defined by the presence of a polarizing beam splitter (PBS). The light that reaches the Pockels' cell then has a defined state of polarization. A certain amount of voltage is applied to the Pockels' cell so as to change the property of the crystal (i.e. index of refraction) such that the optical resonator is capable of switching from a high Q to a low Q state. The Q factor of the resonator is therefore dependent on the amount of voltage applied. In the high Q state, QS pulse is produced, whereas in a low Q, the light deserts the cavity through the PBS.

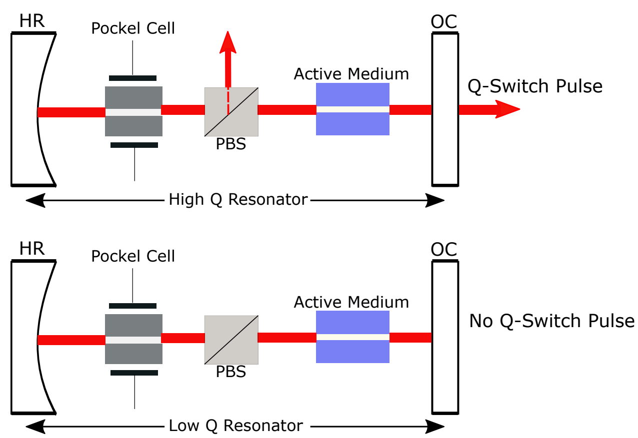

Figure 4.1: General configuration of a cavity resonator with a Q-switch

It is important to take a moment here and express a partial qualitative understanding of how the nonlinear crystal works. In an isotropic material there is a linear relation between the polarization of the medium and the applied electric field ($\vec{P} = \chi\ \vec{E}$), where χ is the electric susceptibility of the material. The crystal structure inside the Pockels' cell is however nonlinear, in the sense that the optical properties of the crystal vary with an applied electric field, inducing a linear electric effect between the index of refraction of the medium and the electric field applied. The relationships given in equations 4.1 to 4.3, between the applied electric field $\vec{E}$ with the induced polarization in the crystal $\vec{P}$ [28], show that each polarization components now depends on the three electric field's components. The Pockels' cell takes advantage of this nonlinear property of the polarization to control and change the polarization state of the laser resonator for the generation of a Q-switch pulse.

$$P_x = \varepsilon_0 \left(\chi_{11}E_x + \chi_{12}E_y + \chi_{13}E_z\right) \tag{4.1}$$

$$P_y = \varepsilon_0 \left(\chi_{21}E_x + \chi_{22}E_y + \chi_{23}E_z\right) \tag{4.2}$$

$$P_z = \varepsilon_0 \left(\chi_{31}E_x + \chi_{32}E_y + \chi_{33}E_z\right) \tag{4.3}$$

The functionality of a Pockels cell is more or less similar to how waveplates made with two refracting crystals, operate. In the case of a quarterwave (λ/4) plate for instance, a propagating light is forced to slow down inside the crystals that make up the waveplate, as it now sees two different indexes of refraction, called fast and slow axes, or ordinary (o) and extraordinary (e) axes. Two different waves are then generated and travel at different speed of light such that there is now a phase difference, ϕ, between their respective polarization. The phase shift ϕ is dependent on the thickness T of the crystal, where:

$$T = \frac{\lambda}{4}\left(\frac{1}{n_o - n_e}\right) \tag{4.4}$$

n_0 and n_e are the indexes of refraction the light sees as it propagates along the ordinary and extraordinary axes, respectively. A λ/4 waveplate in general generates a 90 $^\circ$ phase shift between the waves. In the case of a Pockels cell, the index of refraction is changed by applying a DC voltage to the cell that induces the required phase shift.

A schematic of the different possible Q-switching configurations is presented in figure 4.2. The first two configurations (A & B) are referred to as Quaterwave configurations in the sense that, they create a $\pi/2$ phase difference between the two propagating components of the light field. The only difference between these two configurations is that configuration A requires an applied

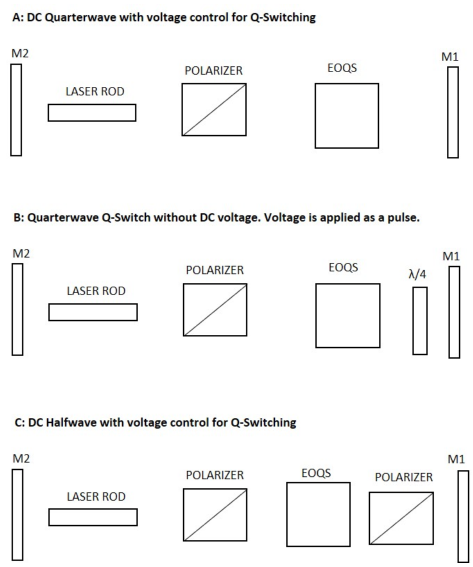

Figure 4.2: Q-Switching configuration of a cavity resonator with a Q-switch

DC quaterwave voltage to prevent lasing, but only utilize few optical components. The advantage of using configuration B however, is that no DC voltage is needed because the quaterwave plate provides the necessary optical bias. In configuration C, the DC voltage is also required but it is a halfwave configuration because it creates a phase difference of $\frac{\lambda}{2}$ between the polarization states of the light. The second configuration is implemented in the experiment.

4.2 Q-Switch YAG Lasers

An important parameter to consider when working with Pockels' cells in an optical resonator, is deciding which crystal is adequate for the laser resonator in question [34]. Pockels' cells are capable of changing the state of the system within a few nanoseconds compared to any mechanical devices previously used to produce short pulses. However, to be implemented in a laser resonator, the Pockels' cell requires not only a crystal that has low losses but also is able to withstand the generated high peak pulses, to avoid risk of damage. In the illustration of the experimental set-up shown in figure 4.3 for the 1064 nm and 1319 nm YAG lasers, a KDP and a BBO crystal are used for Q-switching, respectively. More details about the crystals' internal properties are found in subsequent chapters but table 4.1 shows physical parameters of each crystal.

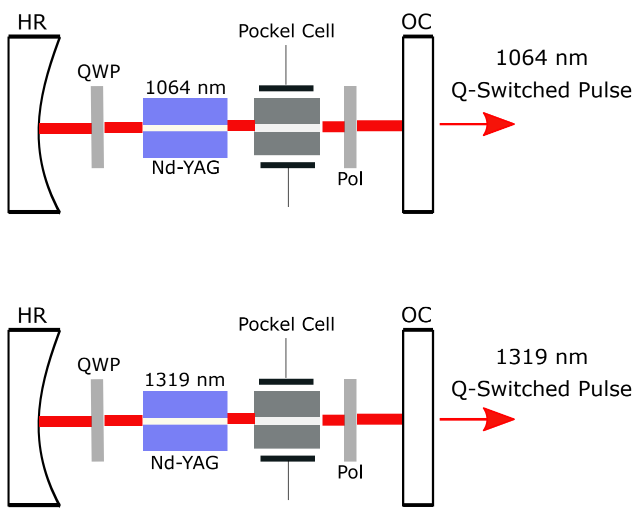

Figure 4.3: Q-Switched Pulse Lasers

Physical Parameters	**BBO Crystal**	**KDP Crystal**
Dimensions (mm)	3 $\times$3 $\times$25	housing diameter 35 $\times$ length 47.5
Aperture (mm)	2.5	10
Quaterwave Voltage (KV)	3.6	3.4

Table 4.1: Physical parameters for BBO and KDP Crystals

Going back to figure 4.3, the light from the high reflector (HR) passes through the $\frac{\lambda}{4}$

waveplate, and as mentioned earlier, the waveplate creates two beams that propagate with a $\pi/2$ phase shift between them, such that the light is now said to be circularly polarized. The circularly polarized light then enters the Pockels' cell that has an applied high voltage (HV) corresponding to a quaterwave retardation. The QS drivers are capable of supplying 0.5-5 KV. For the KDP crystal, the required HV is 3.4 KV for a quaterwave configuration, while 3.6 KV is necessary for the BBO crystal. The Pockels' cells and their drivers are purchased from FastPulse Technology Inc. If the appropriate QWV is supplied to the Pockels' cell, the circular polarization of the light is changed into linear polarization, and a short output pulse is produced as the light exits the Pockels' cell. As this pulse enters the polarizing beam splitters, light gets linearly polarized in only one direction (either horizontally or perpendicularly). As already mentioned in the introductory section of this chapter, the observation of a pulse indicates that the cavity has a high Q value. Figures 4.4 and 4.5, show the actual Q-switch configurations set-up for both 1064 nm and 1319 nm YAG lasers, respectively.

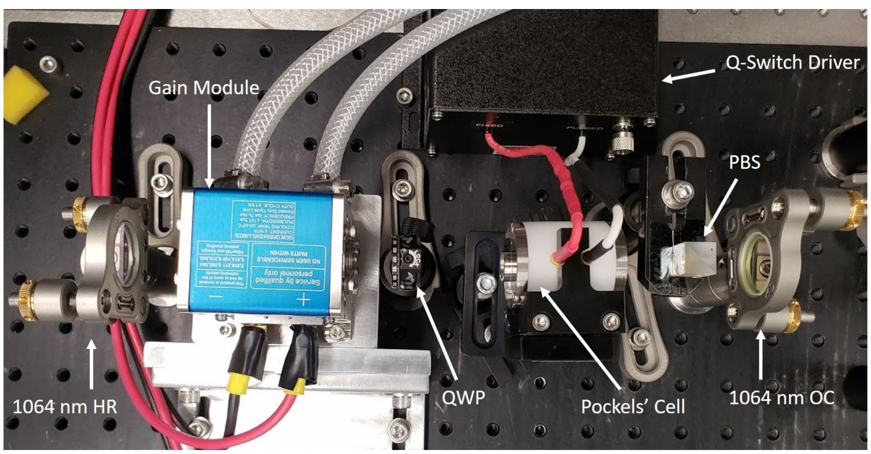

Figure 4.4: 1064 nm laser cavity Q-Switching configuration

The remainder of this section is focused on the experimental set-up and analysis of the obtained Q-switched pulses. There are several experimental conditions necessary to follow to produce a Q-switch pulse. The first condition is to properly align one of the axes (X or Y) of the QS crystal along the same direction of the optic axis of the ND:YAG resonator. Alignments are made

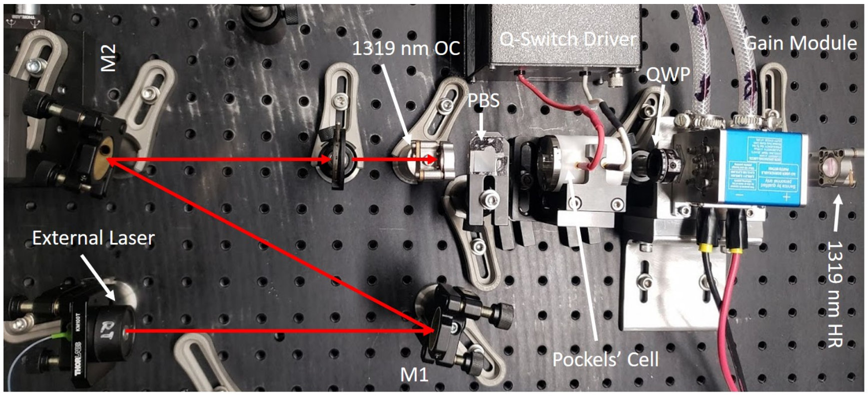

Figure 4.5: 1319 nm laser cavity Q-Switching and alignment configuration

with ≤ 1 W laser power. In the case of the Pockels' cell for 1064 nm laser, the crystal sits inside an enclosure that has windows on each side of the crystal. As the light goes through the Pockel's cell, there are three observed reflections. Two of those reflections come from the windows reflections, and only one of the three reflections is related to the crystal. This is the beam that needs to be aligned with respect to the cavity. A general rule of thumb is, the faintest beam corresponds to the reflection off the crystal.

Regarding the Pockels' cell for the 1319 nm laser, because the resonator is made of mirrors with smaller diameters, and also because the aperture of the BBO crystal is only about 2.5 mm as presented in table 4.1, the use of an external laser is required for proper alignment. Figure 4.5 illustrate how the alignment of the Pockels' cell is done. First, the light from an external laser is passed through the cavity without the Pockels' cell. The mirrors, M_1 and M_2, are used to adjust the height and longitudinal axis of the beam. Then the Pockels' cell is inserted within the cavity and placed such that the maximum output of the external beam is transmitted through the cell.

Once the alignment is performed, the Pockels' cells are connected to their respective Q-switch drivers through the HV output wires (HOW), the second condition for obtaining a QS pulse is performed. This condition is related to the laser hold off. The optical resonator is set to operate at slightly above a particular current called the hold-off current. To determine what current setting to use, the Q switch is turned off and the pump power is slowly increased while adjusting the $\frac{\lambda}{4}$ waveplate to block lasing. The pump current at which the laser resonator can no longer stop lasing is the current at which the gain medium needs to be pumped. Both Nd:YAG lasers are currently being pumped with a current of about 40 Amps and a pulse width of 150 us.

Finally, the last condition necessary to generate a Q-switch pulse is to first apply a trigger signal to the Q-switch and then, synchronize this Q-switch trigger with the pump laser pulse, while creating a time delay between the trigger pulse and the pump pulse. A timing diagram for the lasers is represented in figure 4.6. The system is synchronized to a time T_0. At T_0, a trigger is sent to the lasers pump diode with a pulse width of 150 μs. A trigger is then sent to the QS with a delay of 145 μs from the time T_0. Due to propagation delay, Pockels' cell is switched on about 50 ns after the trigger. To implement the time delay the timing diagram illustrates, connections shown in figure 4.7 are observed.

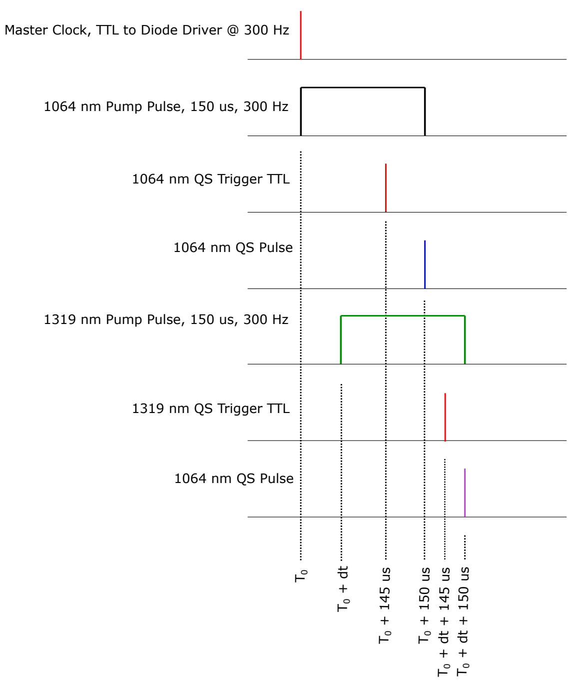

Figure 4.6: Timing diagram for 1064 nm and 1319 nm pump lasers

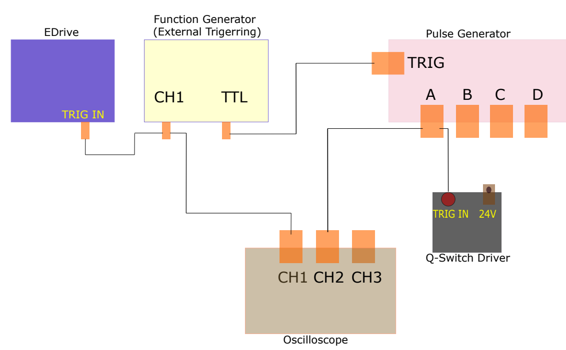

Figure 4.7: Time delay set up

A function generator, a pulse generator, an oscilloscope, and the PDA36A silicon detector are used in the set-up, and connected from one another by means of BNC cables. Using a T-connector, the output connector of the function generator is connected to both channel 1 of the oscilloscope and the trigger gate of the eDrive controller to produce external triggering of the gain medium. A 50 Ω terminator is added to create impedance matching between scope and the function generator. The TTL connector of the function generator is used for synchronization. It is connected to the trigger connector of the pulse generator. The pulse generator has multiple channels (A,B,C and D). Another T-connector is attached to channel A of the pulse generator. One end of the T-connector is connected to channel 2 of the oscilloscope and the other end is joined to the QS input trigger. The photodiode detector is connected to channel 3 of the scope, which is where a QS pulse is observed.

Let us now discuss the importance of each of these experimental requirements. First and foremost, the alignment of the Pockels' cell inside the optical cavity is crucial because improper alignment or adjustment of the QS could result in a poor execution of Q-switching. As shown in figure 4.8, the appearance of after pulses are an indication that either the Pockels' cell is not well aligned or the polarization axis between the Q-switch and the quarterwave plate are not parallel to one another. These after pulses are therefore eliminated by adjusting the alignment of the Q-switch and by rotating the quarter-waveplate. The next figure (figure 4.9) shows the importance of synchronizing the laser pulse with the input trigger pulse of the QS. If the QS pulse trigger is properly synchronized to the laser pulse, only one Q-switch pulse is observe on the time trace of the oscilloscope. Figure 4.9 however, shows multiple pulses which are caused by asynchronous pulses. The QS pulse is analyzed in Mathematica by fitting it to a Gaussian.

A time delay between the QS pulse (for both 1064 nm and 1319 nm lasers) and the pump laser pulse is equally important. As seen in the diagram of figure 4.6, the Q-switch is triggered

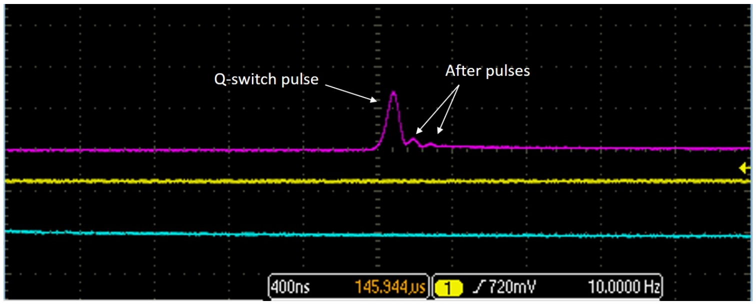

Figure 4.8: Demonstration of after pulses obtained from cavity misalignment

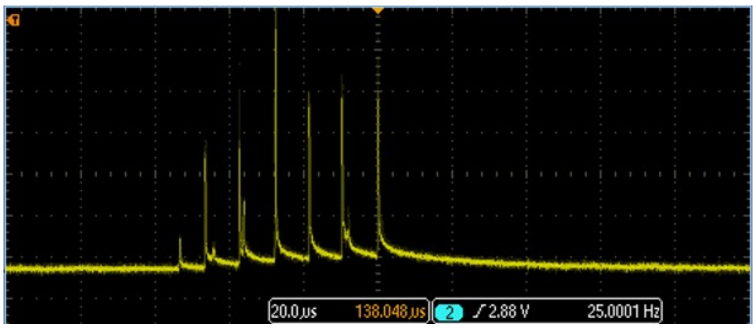

Figure 4.9: Ringing caused by timing error

at time $T_0 + 145\mu$s which is nearby the falling edge of each pump pulse. This is to ensure that the YAG lasers have stored sufficient amount of energy in the gain medium before the Q-switch is switched on for the generation of a QS pulse. Lower time delays do not provide a high peak QS pulse. In figure 4.10, a Q-switch pulse for the 1064 nm pump laser is obtained using a time delay of 147 μs and a YAG pump current of 42 Amps. The blue pulse is the pulse trigger to the Q-switch. The pink pulse is the Q-switch pulse obtained after switching on the Pockels' cell and finally, the yellow line represents the trigger pulse to the YAG laser. It does not appear within the window due to the small time scale of the scope. The scope has been set to trigger on this pulse.

The Q-switch pulse has been further analyzed by fitting it to a Gaussian [35] with the following equation:

$$f(x) = A * \frac{1}{\sigma\sqrt{2\pi}} \exp\left[-\frac{1}{2}\left(\frac{x-\mu}{\sigma}\right)^2\right] + y \tag{4.5}$$

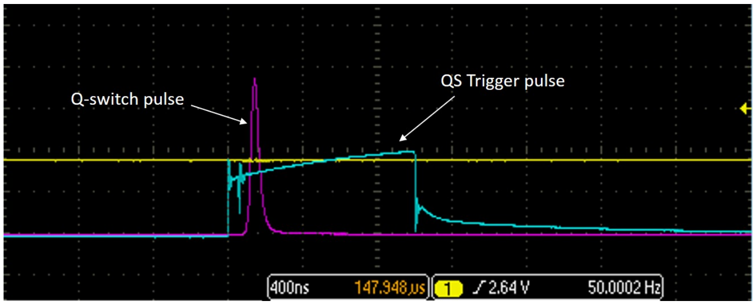

Figure 4.10: A Q-switched pulse from the 1064 nm YAG laser

where the squared of σ is defined as the variance or the square of the Gaussian RMS width. A is the amplitude, μ is the expected value or the position of the center of the peak, and the parameter y is responsible for the offset. Figure 4.11 shows plots of both the obtained QS pulse in red for 1064 nm and the fit in dashed blue. It should be noted that because the actual QS pulse trails off slower at the end, a perfect fit is not achieved since the Gaussian is always symmetric. The values of each variables in equation 4.5 are obtained from the fit and are listed in table 4.2 and the calculated pulse width at FWHM is found to be approximately 50 ns. Note that the width of the QS pulse could be changed by changing the length of the cavity. A power stability of the 1064 nm laser is performed when the laser is Q-switching. The result of the stability curve in figure 4.12 shows a lot of fluctuations. The fluctuations are observed to occur from mechanical vibrations around the lab. Whenever someone would walk close to the system for instance, high peaks would occur in the data recording. This problem could be solved by implementing vibration isolators onto the optical table. The calculated standard deviation is still relatively low, compared to measurements presented in chapter 3.

Variables	**Values**
σ	2.19×10^{-8}
μ	1.47^{-4}
A	9.99×10^{-8}
y	4.50^{-2}

Table 4.2: Gaussian fitting parameters

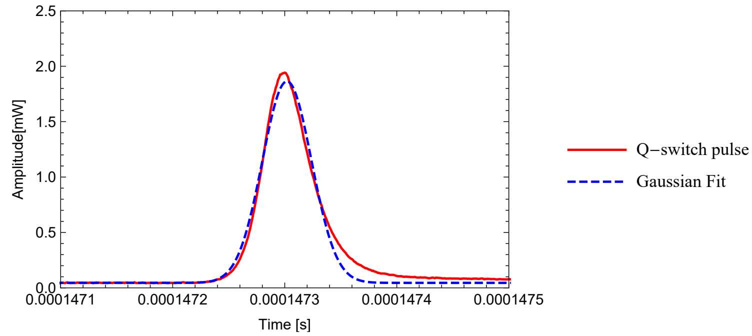

Figure 4.11: Q-switch pulse from the 1064 nm YAG laser fitted to a Gaussian

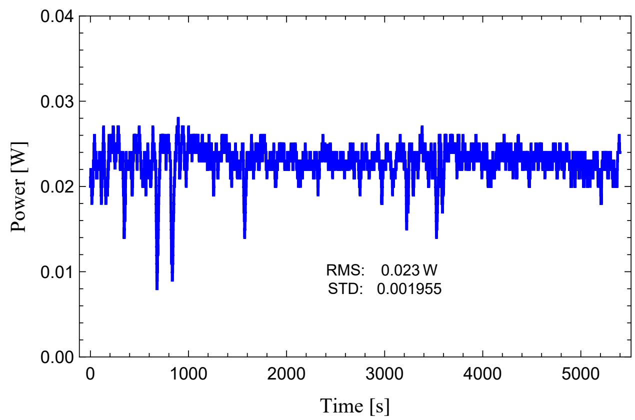

Figure 4.12: Power stability of the Q-switched 1064 nm YAG laser

Regarding the QS pulse for the 1319 nm, recall that the crystal inside the Pockels' cell is a BBO [36], and it requires a HV of 3.6 KV. The detector used to observe this pulse is the Thorlab DET10N2 biased detector. The same configuration as in figure 4.7 and same parameters are used, compared with the 1064 nm system: 1 μs QS pulse trigger, 50 Hz repetition rate, and a pump pulse width of 150 μs. When the HV is applied a sharp pulse appears on the scope, considering that cavity alingment is well done. Figure 4.13 shows the oscilloscope's screen shot of the obtained pulse along with the QS trigger pulse.

The QS pulse for 1319 nm is also fitted to a Gaussian as presented in figure 4.14, and the

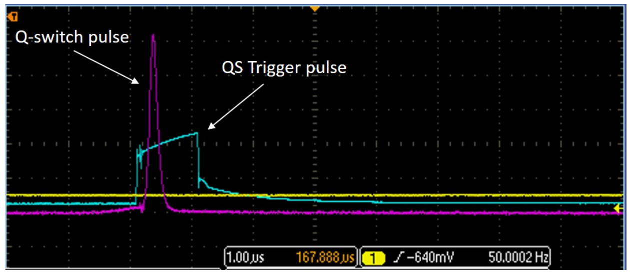

Figure 4.13: A Q-switch pulse from the 1319 nm YAG laser

fitted parameters are listed in table 4.3. The pulse width at FWHM is found to be approximately 200 ns, almost four times as big as the obtained pulse for 1064 nm YAG laser. Because the two QS pulses have to be mixed for SFG, they need to be overlapped both spatially and temporally. Having one pulse that is much bigger than the other will cause a drop in the conversion efficiency. Therefore, the QS pulse obtained with the 1319 nm YAG laser needs to be improved.

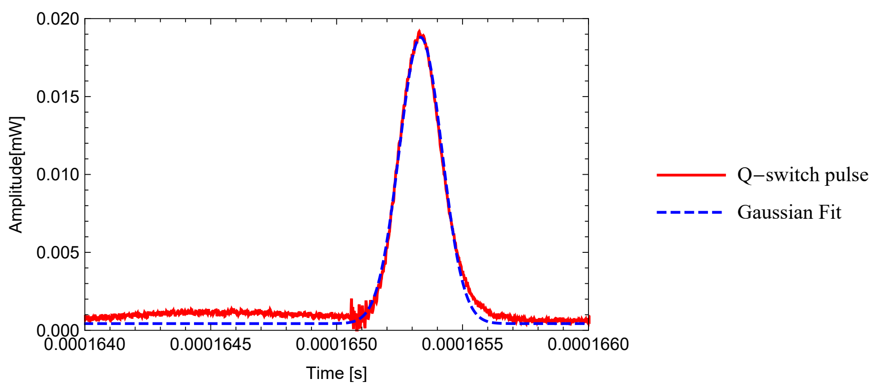

Figure 4.14: Q-switch pulse from the 1319 nm YAG laser fitted to a Gaussian

Variables	**Values**
σ	8.48×10^{-8}
μ	1.65^{-4}
A	3.90×10^{-9}
y	4.30^{-4}

Table 4.3: Gaussian fitting parameters

4.3 Limitations of Q-switching (Mode Locking)

A remarkable aspect of Q-switching is its ability to change the quality factor of a cavity in a fraction of nanosecond to produce a pulse with a pulse width in this scale. However, there is another technique that is capable of producing even shorter pulses. This technique is known as mode-locking. Just like Q-switching, modelocking techniques are categorized as active and passive. Both techniques are capable of generating picosecond $1(ps) \equiv 10^{-12}$s pulse duration laser light to femtosecond pulses, with high peak power equal to $N^2E_0^2$, where N is the number of modes that are oscillating within the laser cavity at different phases. The modelocking, as suggested by the name, locks these cavity modes such that they oscillate at a single phase, therefore increasing the peak intensity of the laser by a factor N larger compared to the average intensity of the number of modes N that are oscillating at arbitrary phases. As it is outside of the scope of this thesis, the reader is suggested to refer to [23, 37, 38] for further information on modelocking techniques.

CHAPTER 5

SUM-FREQUENCY GENERATION AT 589 NM

Second-harmonic generation, sum- and difference frequency generation, third-order frequency generation, or stimulated Raman scattering, are all nonlinear optical processes that are caused by a strong electric field light propagating inside a nonlinear medium [16, 23, 39, 40]. An example of a source of such intense field is a laser, which is capable of producing $\approx 10^{20}\left(\frac{W}{cm^2}\right)$ of power per centimeter area. This chapter covers the principle of nonlinearity and describes the sum-frequency conversion implemented in the experiment for both high and low power frequency conversion.

5.1 Sum-Frequency Conversion (SFG)

Sum-frequency generation is illustrated in figure 5.1. Two frequencies, ω_1 and ω_2 are launched into a nonlinear crystal that carries the second-order electric susceptibility χ^2. The output wave frequency, ω_3 is the sum of the two input frequencies. The input electric fields can be written in terms of the propagating field as:

$$E_i(z,t) = A_i e^{i(k_i z - \omega_i t)} \tag{5.1}$$

for $i = 1, 2$. A_i represents the amplitude of the waves and is a function of the propagation distance z.

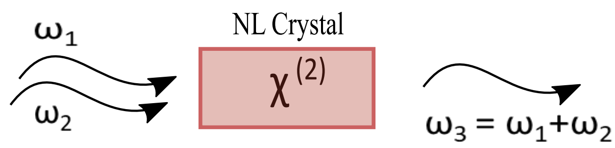

Figure 5.1: Illustration of sum-frequency generation in a nonlinear crystal

The electromagnetic wave equation in this nonlinear material is then given by:

$$\nabla^2 \tilde{\mathbf{E}}_i - \frac{\varepsilon^{(1)}(\omega_i)}{c^2} \times \frac{\partial^2 \tilde{\mathbf{E}}_i}{\partial t^2} = \frac{1}{\varepsilon_0 c^2} \frac{\partial^2 \tilde{\mathbf{P}}_i^{(NL)}}{\partial t^2} \tag{5.2}$$

Considering that a nonlinear process occurs inside the crystal, the polarization of the generated frequency ω_3 is,

$$\tilde{\mathbf{P}}(z,t) = P_3 e^{-i\omega_3 t} + c.c. \tag{5.3}$$

where $P_3 = 4\varepsilon_0 d_{eff}(E_1 E_2)$. The electric field representation of $\tilde{\mathbf{P}}$ is $\tilde{E_3}(z,t) = A_3 e^{i(k_3 z - \omega_3 t)} + c.c.$. Substituting for $\tilde{E_3}(z,t)$ and $\tilde{\mathbf{P}}(z,t)$ into the nonlinear wave equation in 5.10, a series of mathematical derivations and approximations lead to the expression of the spatial variation of each field [16].

$$\frac{dA_1}{dz} = \left[\frac{2id_{eff}\omega_1^2}{k_1 c^2}\right] A_3 A_2^* e^{-i\Delta kz} \tag{5.4}$$

$$\frac{dA_2}{dz} = \left[\frac{2id_{eff}\omega_2^2}{k_2 c^2}\right] A_3 A_1^* e^{-i\Delta kz} \tag{5.5}$$

$$\frac{dA_3}{dz} = \left[\frac{2id_{eff}\omega_3^2}{k_2 c^2}\right] A_1 A_2 e^{-i\Delta kz} \tag{5.6}$$

Equations 5.12 through 5.14 describe the spatial variation of the waves with frequency ω_1, ω_2, ω_3, respectively. The amplitudes of the input waves, A_1 and A_2, are assumed to be constant relative to the amplitude of the SFG wave, A_3. The input waves are therefore said to be undepleted.

The Δk term appearing in each of the spatial variation equations is called the wavevector mismatch for SFG and is used to set phase matching conditions for frequency conversion, as follows:

$$\Delta k = k_1 + k_2 - k_3 \tag{5.7}$$

In terms of refractive indexes, 5.15 is rewritten as

$$\frac{n_1 \omega_1}{c} + \frac{n_2 \omega_2}{c} = \frac{n_3 \omega_3}{c} \tag{5.8}$$

where $\omega_3 = \omega_1 + \omega_2$. Also note that in this case, k_1, k_2, k_3 are considered to be collinear.

Phase matching conditions [16, 41, 42] are guidelines to produce nonlinear processes such as SFG. There are two cases for phase matching: Δk = 0 for perfect phase matching, and, Δk $\neq$ 0 for non-critical phase matching. In the case of perfect phase matching, the electromagnetic wave with frequency ω_3 is linearly proportional to the direction of propagation z, such that there is a constant phase relation between $\tilde{E}$(z,t) and $\tilde{P}^{NL}$(z,t). The intensity of the generated wave is therefore equivalent to the input frequencies. If the phase matching condition in 5.15 is not equal to zero, the amplitude A_3 of the generated field at the output of a nonlinear crystal of length L is given as:

$$A_3(L) = \left(\frac{2id_{eff}\omega_3^2 A_1 A_2}{k_3 c^2}\right)\left(\frac{e^{i\Delta kL} - 1}{i\Delta k}\right) \tag{5.9}$$

From equation 5.16, the intensity I_3 is then,

$$I_3 = \left[\frac{8n_3 \varepsilon_0 d_{eff}^2 \omega_3^4 |A_1|^2 |A_2|^2}{k_3^2 c^2}\right]\left|\frac{e^{i\Delta kL-1}}{\Delta k}\right|^2 \tag{5.10}$$

where $\left|\frac{e^{i\Delta kL-1}}{\Delta k}\right|^2$ is also rewritten as $L^2 Sinc^2\left(\frac{\Delta kL}{2}\right)$. Recall that the intensity of a light wave is related to its amplitude by the following equality:

$$I_i = 2n_i \varepsilon_0 c |A_i|^2 \tag{5.11}$$

Therefore the intensity I_3 of the sum-frequency wave is rewritten as,

$$I_3 = \left[\frac{8d_{eff}^2 \omega_3^2 I_1 I_2}{n_1 n_2 n_3 \varepsilon_0 c^2} \right] L^2 Sinc^2 \left(\frac{\Delta k L}{2} \right) \tag{5.12}$$

The expression of I_3 in equation 5.20 allows one to determine the dependence of the efficiency of SFG, when there is a phase mismatch (Δ k $\neq 0$). As it is noted from the term $Sinc^2 \left(\frac{\Delta kL}{2}\right)$, the sum-frequency conversion efficiency depends on both Δk and the length L of the crystal. The efficiency decreases when $|\Delta k| L$ increases. This dependence in L is represented by the coherence length such that,

$$L_{coh} = \frac{2}{\Delta k} \tag{5.13}$$

For $L_{coh} > \frac{1}{\Delta k}$, a phase mismatch occurs between the SFG wave and the input waves. Consequently, the phase matching condition in 5.16 cannot be attained.

However, taking advantage of the birefringence properties of uniaxial crystals [43] as stated earlier, the indexes of refraction of the medium are manipulated such that the polarization of the waves are forced to match.

To achieve birefringence phase matching for SFG using uniaxial crystals, there are a set of conditions put forward. First, $\omega_1 < \omega_2 < \omega_3$, such that the SFG wave with frequency ω_3, is polarized in the direction with the lowest refractive index. Secondly, the type of uniaxial crystal needs to be considered, whether it is a positive or a negative uniaxial crystal.The phase matching condition for each type is given in table 5.1. As the table shows, the SFG wave has to be polarized

Type of Crystal	Positive Uniaxial ($n_e > n_o$)	Negative uniaxial ($n_e < n_o$)
Type I	$n_3^o \omega_3 = n_1^e \omega_1 + n_2^e \omega_2$	$n_3^e \omega_3 = n_1^o \omega_1 + n_2^o \omega_2$
Type II	$n_3^o \omega_3 = n_1^o \omega_1 + n_2^e \omega_2$	$n_3^e \omega_3 = n_1^e \omega_1 + n_2^o \omega_2$

Table 5.1: Uniaxial Crystals' Phase Matching Conditions

in the ordinary axis if using positive uniaxial crystals, and in the extraordinary axis for negative unaxial crystals, such that in both cases, the generated wave propagates in the lowest refractive index region of the medium. One also notes that in a type I uniaxial crystal, the two propagating input waves have the same polarization but in Type II, they are orthogonal from each other.

Phase matching the polarization of the waves in order to obtain high conversion efficiency, requires techniques such as angle tuning or temperature tuning. The discussion is reduced to temperature tuning because the birefringence of the crystals implemented in the experiments is heavily dependent on temperature.

Some of the important properties of the crystals used for the experiments discussed in this are listed in table 5.2. Potassium dihydrogen phosphate (KDP) or KD*P crystals have

Crystal	Uniaxial (+ve or -ve)	d_{eff} (pm V^{-1})	Temperature ($^\circ$ C)
KD*P	-ve	0.38	13
$LiNbO_3$	-ve	5.89	1.1
BBO	-ve	2.01	50

Table 5.2: Properties of the nonlinear crystals

considerably low electro-optics coefficients with $d_{36} = 0.44$ pm V^{-1} for KDP and $d_{36} = 0.38$ pm V^{-1} for KD*P. The value of electro-optics coefficients of Lithium niobate ($LiNbO_3$) crystals at d_{31} and d_{22} are -5.4 and 2.8 pm V^{-1}, respectively. $LiNbO_3$ crystals have excellent chemical and mechanical properties but have low damage threshold. On the other hand, Barium borate (BaB_2O_4) crystals, also called BBO crystals, have high damage threshold but low coeffiecients $d_{22} = 2.2$ pm V^{-1} and $d_{31} = 0.16$ pm V^{-1}.

5.2 High Power SFG

In this section, the development of a nanosecond pulsed laser system resonating at sodium wavelength (589 nm) by means of sum frequency generation (SFG) with Nd:YAG lasers at 1064 & 1319 nm, is presented. The laser is aimed to perform LiDAR measurements [44, 45, 46] at mesospheric altitude and therefore requires an output power of 2-5 W with a pulse width from 1-50 ns. The active Q-switching technique is used to obtained the appropriate pulse widths. The laser designs and characteristics are discussed.

A schematic of the sodium laser is shown in figure 5.2. As illustrated, the two resonators for each pump lasers are implemented to produce sum-frequency generation. The 1064 nm and 1319 nm lasers are placed on a 36 $\times$ 24 breadboard and are parallel to each other. Their respective gain media, waveplates, polarizers and Pockels' cells are placed within the cavities to produce the desired high-power single frequency pump lasers. The 1319 nm laser is half an inch shorter than the 1064 nm due to the height of the mirrors. Therefore, to spatially overlap both laser beams, a system of two-mirrors is built in front of the 1064 nm laser output. The mirrors are mounted on kinematic mounts to obtain some degree of freedom in the motion of the beam. The polarizing beam splitter is placed at the location where the beams meet and its height is adjusted based on the 1319 nm laser output heigth.

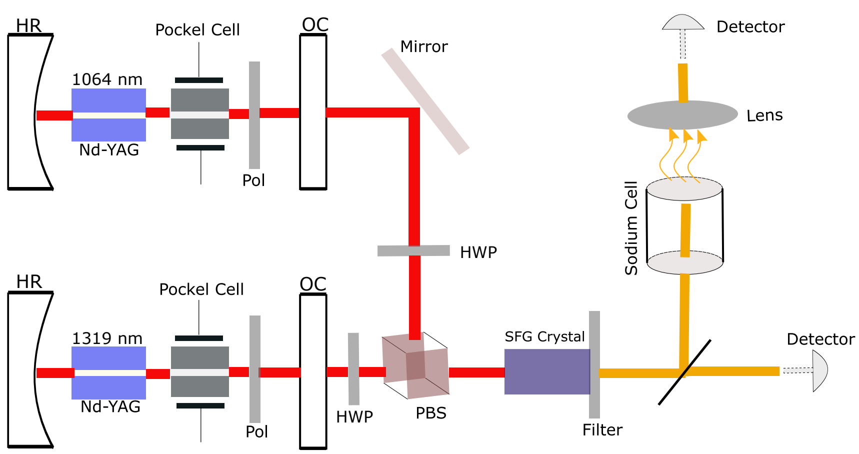

Figure 5.2: Sodium laser Schematic

The need of a half-wave plate along the path of the 1064 nm laser is to rotate the polarization of the beam such that the polarization of the pump lasers are orthogonal to each other for non-critical phase matching in a Type II uniaxial crystal. The polarization of the 1319 nm laser has a horizontal polarization as it exit the PBS so the polarization of the output beam for 1064 nm is made horizontal such that, only perpendicular polarization gets reflected towards the SFG crystal. The SFG crystal is a type II nonlinear crystal. The filter located after the crystal is a bandpass filter. It is placed close to the crystal to filter any unwanted infrared light and only transmits yellow light. The sodium light is then reflected to a sodium cell for spectroscopy measurements.

5.3 Low Power SFG

In the previous chapter, sum-frequency is performed in free-space by spatially and temporally overlapping the high-power pump lasers inside a nonlinear crystal. In this section, the mixing of the two pump lasers occurring in a waveguide [47, 48, 49] is discussed.

As it is discussed earlier, the generation of nonlinear processes requires high intensity beams. Another way of producing beams with high intensities is by focusing them into a waveguide such that the tight confinement in a smaller region, produce a high intensity necessary for enhanced nonlinear effects. The lasers used to perform this experiment are low power DFB lasers, with single wavelengths at 1064 nm and 1319 nm.

The 1064 nm laser is a Qphotonics fourteen-pin butterfly laser diode mounted on the QSDIL-300 laser driver for temperature control. It has a threshold current of 30 mA with required TEC current of 1.2 A. Its pin configurations matches those of type I pin configuration. The 1319 nm is also a 14 pin butterfly laser diode from NTT but with type II pin configuration. The maximum threshold current for the 1319 nm diode laser is 20 mA, with an expected fiber output power of 31.7 mW. The controller for this laser is purchased from Newport with the LDM-4984 laser diode mount that gives the flexibility to change configuration form type I to type II pin configuration, depending on the need, see figure 5.3 and 5.4. The wires are then connected for type II. The controller. The PID values on the controller are set to 0.2008, 0.1972, and 0.0010, for P, I and D.

respectively.

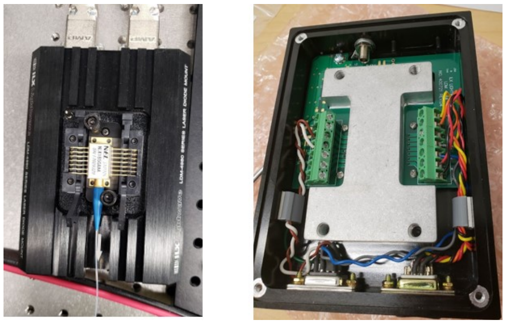

Figure 5.3: Top and bottom configuration of the 1319 nm laser diode mount

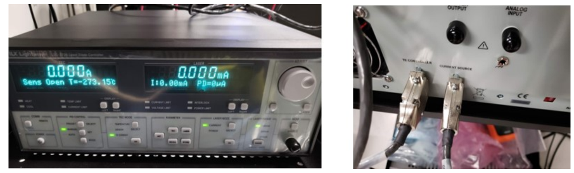

Figure 5.4: Laser diode controller, front and back panels

A waveguide mixer is obtained from HCP corporation to perform sum-frequency generation with the two diode lasers mentioned earlier. Port 1 in figure 5.5 corresponds to the 1064 nm input, port 2 is the input port for 1319 nm, and port 3 represents the 589 nm output. Both DFB lasers are then attached to the HCP waveguide on their respective ports. A filter is place after port three to block any unwanted radiation and a yellow light is observed on a white piece of paper.

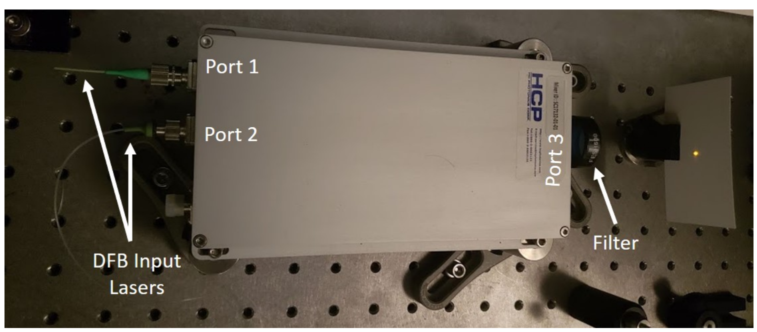

Figure 5.5: Waveguide SFG: 1064 nm + 1319 nm

Though a temperature controller for the HCP waveguide is needed for a better conversion efficiency of this system, temperature tuning is performed by changing the temperature of the 1064 nm DFB laser upon changing the resistance of the thermistor. A plot showing the dependence of the SFG output power with respect to resistance is represented in figure 5.6. The plot shows that a maximum output power is obtained at a resistance of 8.9 kΩ and Below or above this value, there is a decrease in power, which is an indication that the input beams are walking away from one another rather than mixing along the same propagation axis, which in turn causes a poor conversion efficiency.

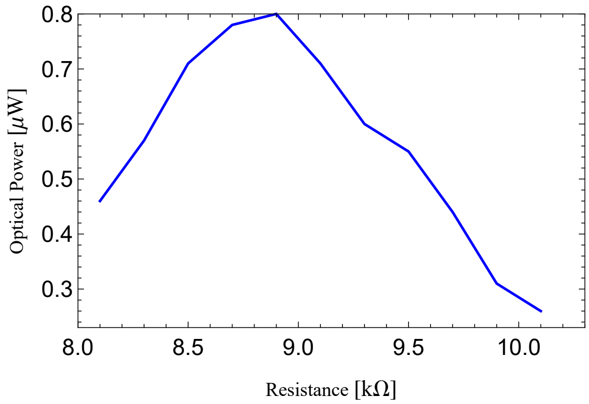

Figure 5.6: Temperature tuning of the 1064 nm DFB laser in terms of SFG output power

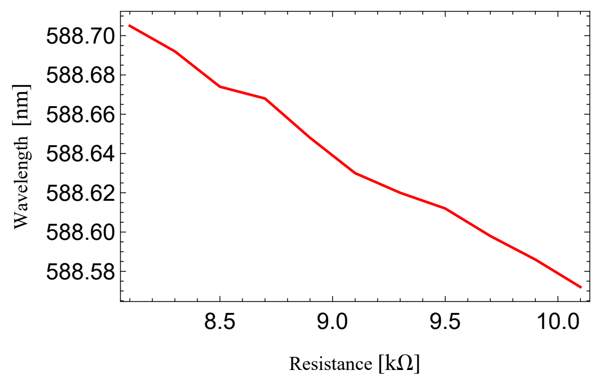

Figure 5.7: Temperature tuning of the 1064 nm DFB laser in terms of wavelength

In figure 5.7 on the other hand, the wavelength is recorded and plotted in terms of change in resistance. The plot shows that a lower resistance (or temperature) is needed in order to obtain the 589 nm yellow light at sodium resonance. The plot therefore demonstrate the need of implementing a temperature control on the waveguide itself. It is noted that changes in temperature in the 1319 nm laser system did not make much of a difference in the results presented.

5.4 Injection Seeding

Injection seeding [50, 51, 52, 53] is used in multiple laser systems to tune a laser at a specific wavelength. The use of a single frequency diode laser is often implemented to perform injection seeding [13, 1, 54]. The DFB lasers presented in the previous section would later on be tuned to sodium resonance and used to perform injection seeding into the high power YAG system.

CHAPTER 6

SODIUM LASER DESIGN: ALTERNATE APPROACH

The previous chapter described the generation of a sodium laser via sum-frequency generation for LIDAR applications. In this chapter, the characterization of a low power continuous wave (CW) sodium laser for laboratory experiments is discussed. The CW sodium light is obtain via second-harmonic generation (SHG) and quasi-phase matching technique is implemented to improve the conversion efficiency of the Lithium Niobate crystal [55, 56] used in the set-up.

6.1 Second-Order Harmonic Generation (SHG)

The mathematical description of second harmonic generation is not different from the sum-frequency generation, with the exception that the two input waves in SFG is now one single frequency in SHG, $\omega_1 = \omega_2$, and thereupon, $\omega_3 = 2\omega_1$. The polarization dependence of second-harmonic generation in a nonlinear material is given by:

$$\tilde{P}(z,t) = \tilde{P}_1(z,t) + \tilde{P}_2(z,t) \tag{6.1}$$

where the amplitudes P_1 and P_2 of the polarization are:

$$P_1(z) = 4\varepsilon_0 d_{eff} A_2 A_1^* e^{i(k_2-k_1)z} \tag{6.2}$$

$$P_2(z) = 2\varepsilon_0 d_{eff} A_1^2 e^{2ik_1 z} \tag{6.3}$$

The spatial variation of the input wave at ω_1 and the one describing the build-up of the generated wave with frequency $2\omega_1$, are given in equations 6.1 and 6.2.

$$\frac{dA_1}{dz} = \left[\frac{2id_{eff}\omega_1^2}{k_1c^2}\right] A_2A_1^* e^{-i\Delta kz} \tag{6.4}$$

$$\frac{dA_2}{dz} = \left[\frac{id_{eff}\omega_2^2}{k_2c^2}\right] A_1^2 e^{-i\Delta kz} \tag{6.5}$$

where Δk is now equal to $2k_1$ - k_2 and the phase matching condition for SHG is:

$$n(2\omega) = n(\omega) \tag{6.6}$$

Finally, the intensity of the SHG wave is written as:

$$I(2\omega_1) = \left(\frac{2\omega_q^2}{n_2n_1^2c^3\varepsilon_0}\right) I^2(\omega_1)d_{eff}^2L^2sinc^2(\frac{\Delta kL}{2}) \tag{6.7}$$

where I(ω_1) is the intensity of the initial electric field light. If the phase matching condition in equation 6.6 for SHG is achieved, the ratio of the output power to the input power gives the conversion efficiency,

$$\eta(z)\big|_{\Delta\neq 0} = \frac{P_2(z)}{P_1} = \frac{2}{\varepsilon_0n_2c^3A}\left(\frac{d\omega}{n_1}\right)^2 P_1\frac{sin^2(\Delta kz/2)}{(\Delta k/2)^2} \tag{6.8}$$

For a maximum conversion efficiency in which $\Delta k \rightarrow 0$, then the efficiency η is a function of z^2 as,

$$\eta(z)\big|_{\Delta k\rightarrow 0} = \frac{P_2(z)|_{\Delta k\rightarrow 0}}{P_1} = \frac{2}{\varepsilon_0n_2c^3A}\left(\frac{d_{eff}\omega}{n_1}\right)^2 P_1z^2 \tag{6.9}$$

6.2 Quasi-Phase Matching for high-efficiency SHG

A phase mismatch between the input wave and the SHG wave causes the intensity of the second-harmonic to oscillate as expressed by equation 6.7. The conversion efficiency reaches a maximum at the coherence length L_c (= $\frac{\pi}{\Delta k}$) described in the previous chapter, but quickly decays to zero after a propagation greater than L_c. This problem is fixed by using a periodically poled crystal such that the nonlinear coefficient d_{eff} is forced to change sign after a distance L_c, and therefore increasing the P^{NL} term. Recall that the polarization is in terms of the nonlinear coefficient as P = 2 $\varepsilon_0 d_{eff} E^2$ hence, changing the direction of the nonlinear coefficient induces a phase matching between the P and E.

A wave propagating in a crystal with periodicity Λ, now has an oscillating nonlinear coefficient expressed in terms of z as, $d_{eff} = d_0 \sin(K_q z)$, where $K_q = \frac{2\pi}{\Lambda}$ is the wavevector. Therefore, for phase matching, the condition is now written as:

$$\Delta k = K_q = \frac{2\pi}{\Lambda} \tag{6.10}$$

Since the spatial variation of the SHG electric field is written in term of the nonlinear coefficient d_{eff} as, $\frac{dA_2}{dz} = i\frac{d_{eff}\omega}{cn_2}A_1^2 e^{-i\Delta kz}$, substituting for the oscillating coefficient $d_{eff}(z)$ gives the following:

$$\frac{dA_2}{dz} = i\frac{d_0 sin(K_q z)\omega}{cn_2}A_1^2 e^{-i\Delta kz} \tag{6.11}$$

Integrating 6.11 then leads to,

$$A_2(z) = \frac{d_0\omega}{2cn_2}E_1^2\left(\frac{e^{i(K_q-\Delta k)z}-1}{i(K_q-\Delta k)} - \frac{e^{-i(K_q+\Delta k)z}-1}{-i(K_q+\Delta k)}\right) \tag{6.12}$$

For $K^-= Kq - \Delta k$ and $K^+= Kq + \Delta k$, the amplitude of the SHG is written in terms of sine function as:

$$A_2(z) = \frac{d_0\omega}{2cn_2}E_1^2\left[e^{-i\frac{(k_q-\Delta k)z}{2}}\left(\frac{\sin\left[\frac{(K_q-\Delta k)z}{2}\right]}{(K_q-\Delta k)/2}\right) - e^{-i\frac{(k_q+\Delta k)z}{2}}\left(\frac{\sin\left[\frac{(K_q+\Delta k)z}{2}\right]}{(K_q+\Delta k)/2}\right)\right] \tag{6.13}$$

The new phase matching condition requires that K_q - Δk = 0, and hence, K_q = Δk. The second term inside the bracket of equation 6.13 therefore does not provide a significant contribution to the amplitude of the SHG wave, and a valid approximation to the SHG amplitude is written the following way:

$$A_2(z) \approx \left(\frac{\omega(d_0/2)}{cn_2}\right)A_1^2 z \tag{6.14}$$

where the amplitude A_2 in 6.14 is derived by means of quasi phase matching (QPM). The efficiency obtained though QPM technique is given by:

$$\eta(z)\big|_{\Delta k=K_q} = \frac{P_2}{P_1} = \frac{1}{2\varepsilon_0 n_2 c^3 A}\left(\frac{\omega d_0}{n_1}\right)^2 P_1 z^2 \tag{6.15}$$

Note that equation 6.9 and 6.15 are almost identical for the exception that in 6.9, the peak value of the nonlinear coefficient d_{eff} but in equation 6.15, the efficiency is reduced to the use of the average value of $d_{eff} = d_0/2$. Furthermore, as already mentioned, the efficiency in 6.9 is only feasible for a certain length called coherence length L_c. In the next section, Lithium Niobate crystal is implemented for the generation of a low-power sodium laser using quasi phase matching.

6.3 SHG-TA/DFB Laser System

A low power continuous wave (CW) sodium laser is built to perform experimental studies of Sodium spectroscopy with a sodium vapor cell in a laboratory environment. The schemes used to obtain the yellow light is referred to as second-harmonic generation (SHG), as stated earlier. Figure 6.1 is a sketch of the experimental set-up.

The pump laser is a fourteen pin fiber diode laser from QPhotonics with a maximum operating current of 87 mA and a center wavelength at 1177.5 nm. As seen in figure 6.7, it is mounted onto a controller for temperature control and current tuning. The end of the fiber is connected to one end of a fiber isolator to avoid any risk of laser damage due to the back reflection of the light from optical components. The maximum insertion loss of this fiber isolator is 2.30 dB at -5° to 50°, plus a 0.3 dB connector loss. The other end of the isolator is connected to a tapered amplifier (TA).

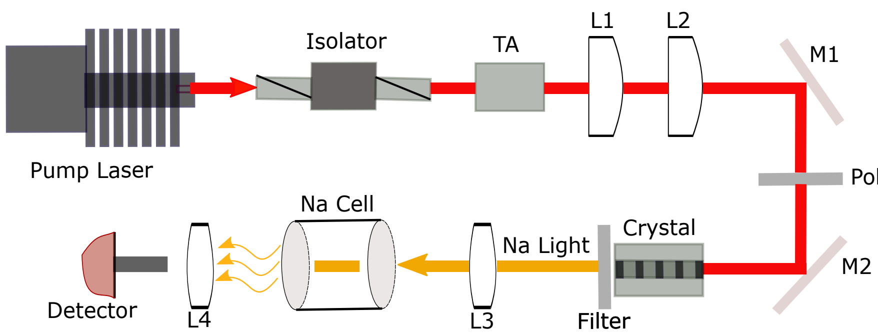

Figure 6.1: Schematics of CW Sodium Laser

The tapered amplifier is a 1 $\times$ 1180 nm module with a TA that sits in a butterfly chassis. The fiber input type of the TA is a PM-fiber and the maximum recommended current is 2 Amps. The tapered amplifier is used to amplify the pump laser power output. Figure 6.2 is a sketch of the interconnections of the TA. The 4308 is connected to the TA to provide current. The 6305 cable carries out a current for both the TEC control of the TA mount, and the ridge waveguide (RWG). The 5240 cable is used to provide TEC control for the internal chip. The C0383 is a three to one head cable that links the TA, the RWG, and the internal TEC, to the TA current controller, the RWG current controller, and the TEC temperature controller, respectively.

The output of the tapered amplifier is free-space, and therefore, light exiting the TA quickly diverges due to diffraction. To fix this problem, a system of two cylindrical lenses are used. The first lens has a focal length of 2.5 cm and is placed horizontally to collimate the horizontal axis of the beam as it diverged faster compared to the vertical. The second cylindrical lens has a focal length of 5 cm and is vertically mounted along the beam's path to fix the vertical divergence of the beam. The collimation of the beam is verified two-meters away from the second lens. Two plane-mirrors with protected gold coating are mounted on kinematic mounts and used to align the beam along the propagation axis of the crystal. The $\lambda/2$ placed along the beam path is used to maximize the power by rotating the polarization of the light to match it with the polarization of the pump laser. L3 is a 25 cm focal length lens used to focus the light into the crystal.

The crystal is a periodically poled lithium niobate crystal purchased from HCP corporation. It is fabricated such that quasi-phase matching is enabled. The crystal physical structure is presented in figure 6.4. As shown, the crystal has multiple gratings with micrometer periods for QPM as, $9.03/9, 14/9.26, 26/9.38$, from left to right. The dimensions of the crystal are given in $X * Y * Z$ as $50 * 2.6 * 0.5$ mm. To achieve the maximum conversion efficiency, the crystal is mounted onto an oven for temperature tuning. At the crystal exit, the FESH600 shortpass filter is placed to block the infrared light.

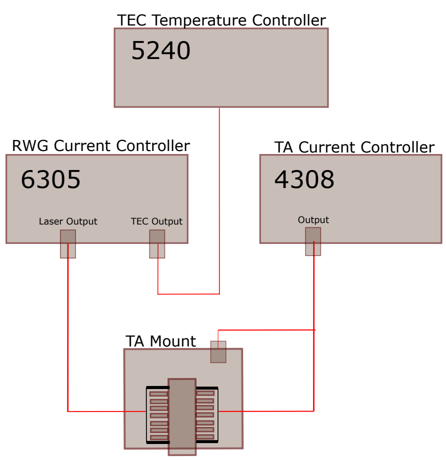

Figure 6.2: Tapered amplifier connections

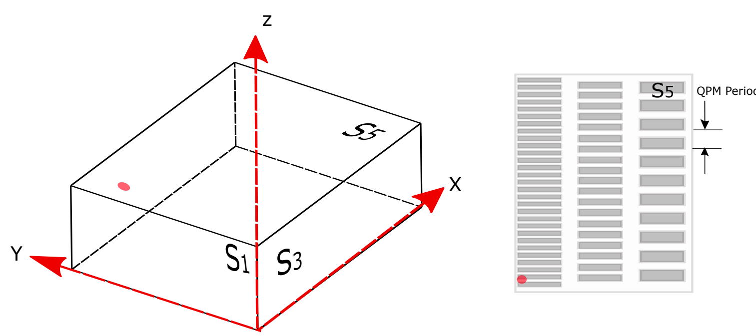

Figure 6.3: PPLN crystal physical structure

Temperature tuning is performed by slowly increasing the temperature of the crystal through the use of a temperature controller connected to the oven. A white paper is placed in after the filter to identify at which temperature yellow light is getting generated. A faint yellow is initially observed at around 40 °C. Then the white paper is replaced by a power meter to record power output versus the crystal's temperature in order to determine the temperature at which maximum conversion efficiency is obtained. Figure 6.5 shows a plot of SHG power in terms of the crystal temperature in Fahrenheit. As noted on the plot, the SHG power decreases for temperatures below and above 83°F. The maximum power, and hence, maximum conversion efficiency is obtained at 83°F. Any further experiments are performed with a crystal's temperature set to this value.

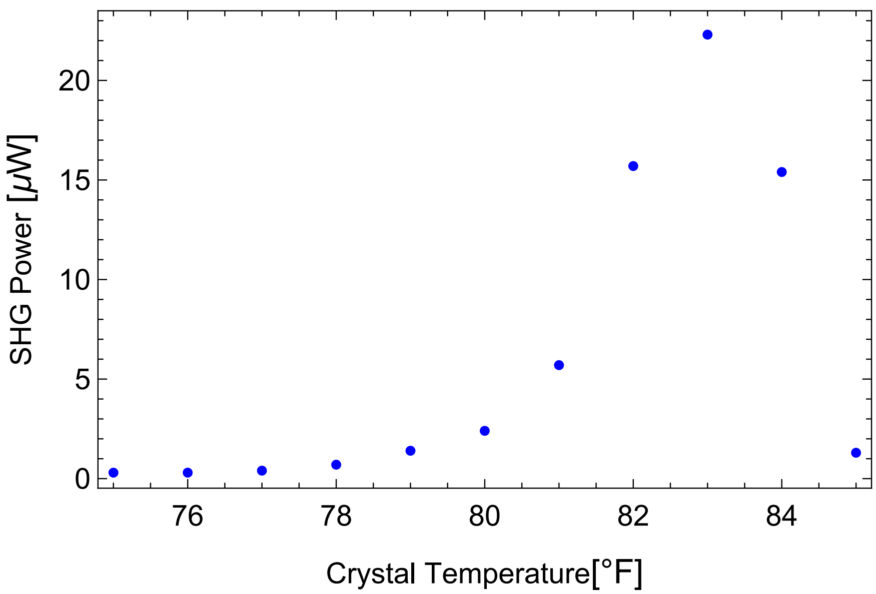

Figure 6.4: Temperature tuning of the CW laser system

The cause of a low SHG power produced is due first, to the small input power from the seed laser. As stated before, it has a maximum operating current of only 87 mA, and producing a maximum power of less than 20 mW. Insertion loss of the fiber isolator further reduced the input power. The power for different currents is recorded and plotted before the fiber isolator and after fiber isolator as shown in figure 6.6, with a 37% difference between the two output power. The calculated insertion loss is about 1.98. This seed laser is not adequate for CW experiment but it is used as a proof of concept and will later be changed. Secondly, the tapered amplifier is currently configured to a maximum current of only 2 Amps, and does not provide sufficient amplification or gain.

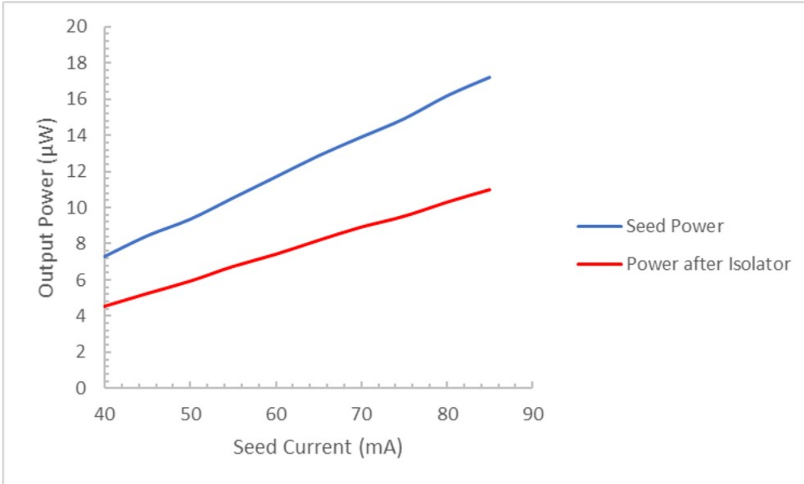

Figure 6.5: Seed power before and after fiber isolator. The center wavelength of the seed laser is about 11778 nm.

Tuning of the seed laser to obtained the sodium D_2 resonance required both a change in temperature and current of the seed laser. Initially, the current is set to a constant value of 83 mA, while the temperature is modulated. Figure 6.7 is a plot of wavelength in terms of seed temperature. The wavelength is recorded using a wavemeter from WaveMaster at a temperature ranging from 28 to 33 degrees.

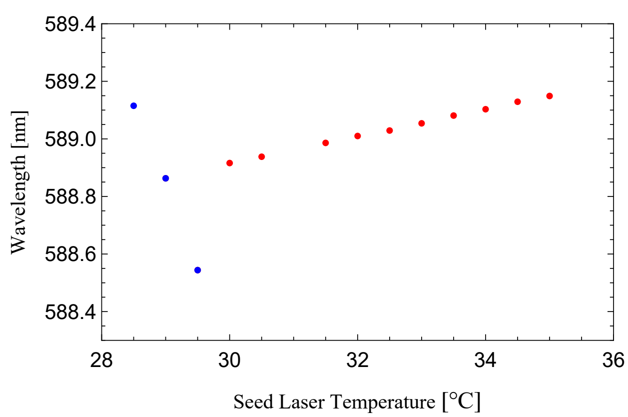

Figure 6.6: Temperature tuning of seed laser. The blue data represent the occurrence of mode hopping at low temperatures

At low temperatures, the data is represented in blue because the wavemeter reading continuously changed from a ’multi-line detection warning’ to an actual value. This may be due to the instability of the laser gain medium at temperatures closed to its internal temperature ($\approx$ °26 C), therefore inducing a phenomenon called mode hoping in which the laser abruptly operates at a different mode than its original mode. Mode hoping of the laser is not detected at higher temperatures.

From figure 6.6, it is obvious that the laser’s temperature should be set to values between 31 and 32 degrees in order to obtain sodium resonance, as these temperatures give approximately 589 nm. The generated second harmonic light obtained through QPM is then sent into a sodium cell as shown in figure 6.7. The sodium cell is a glass tube that contains sodium atoms. To heat-up

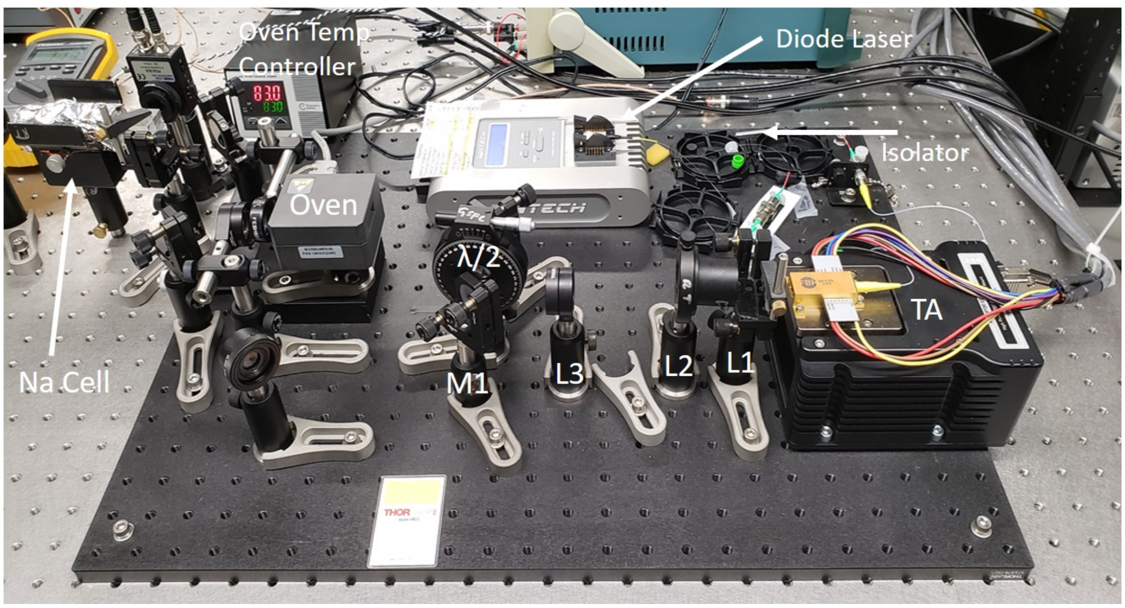

Figure 6.7: Low power CW set-up

the cell up to the sodium atoms melting point (about 98 °C), it is wrapped with an aluminum foil and copper wires to increase heat transfer and conductivity. One end of a nichrome wire is also wrapped around the Na cell while the other end is connected to a DC power supply. The current on the power supply is slowly increased to a current of 1.5 Amps with an output voltage of about 11.98 V. The temperature of the cell is recorded using the HH501DK type K thermometer. For a current of 1.5 Amps, the thermometer read 111 °C ($\approx$ 384 Kelvin).

Once only the cell is heated and a sodium vapor is obtained, that the yellow light is sent into the cell. The temperature of the seed laser is then modulated between 31 and 32 degrees with an increment of 1 °C. Fluorescence from the sodium atoms is observed at a temperature of 32 °C. The light from the Na fluorescence is then focused by a lens into the wavemeter which displayed a wavelength of 589.01 nm. It has been noticed that the wavemeter is off by approximately +0.2 nm, the laser is therefore believed to be at sodium D_2 resonance. Current tuning is used for fine tuning of the wavelength to the third decimal place.

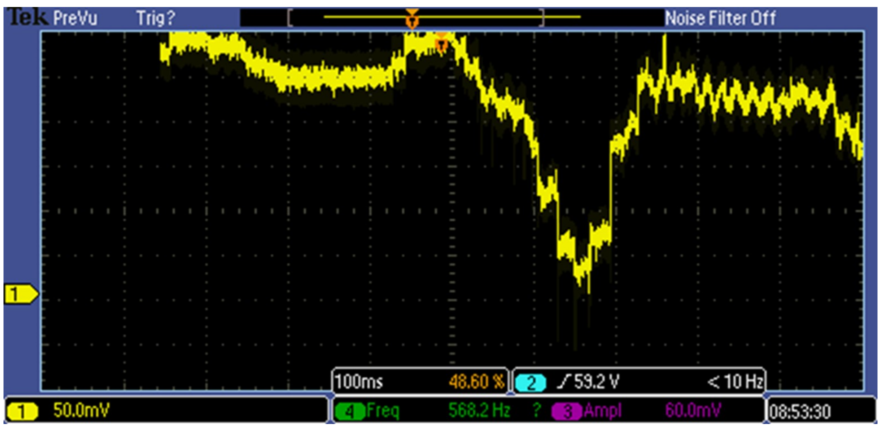

Figure 6.8: Low power CW set-up

Absorption spectroscopy of the transmitted light from the Na atoms is then performed by capturing the light with a lens and focusing it onto a photodiode detector connected to an oscilloscope. It is well known that if a particular set of atomic gas is shone light that carries a defined frequency, say ν_1, the atoms moving along the same direction with velocity v_z, in general will absorb photons if the frequency of the light is $\nu = \nu_1(1+ \frac{v_z}{c})$ [57]. Figure 6.8 shows two dips in the absorption signal from the sodium atoms and the expected D_1 or D_2 transition lines.

CHAPTER 7

CONCLUSION AND OUTLOOK

Sum-frequency sodium lasers for LiDAR applications are a promising apparatus for observational experiments in the Earth's upper atmosphere. The solid-state sodium LiDAR has shown to be capable of providing scientists high-resolution temperature and wind measurement data. This thesis presents in detail the design and characterization of our sum-frequency sodium laser. The thesis also outlines the challenges and changes that need to be implemented in order to produce an efficient sodium laser. We have illustrated the theory behind SFG and have demonstrated sum-frequency generation of sodium resonance radiation by mixing Nd:YAG lasers operating at 1064 nm and 1319 nm.

The work to obtain an efficient conversion of the SFG is still in progress. Future work will include for instance, tuning the frequency of the generated radiation to the D_2 resonance by implementing the injection seeding system explained in section 5.4. However, before injection seed is performed, the DFB lasers need to be temperature tuned by implementing a temperature controller to the HCP waveguide. All of this remaining work will be performed after my thesis defense and therefore the results obtained will not be presented here but in future publications.

REFERENCES

[1] Michael A Krainak, W Yu Anthony, Diego Janches, Sarah L Jones, Branimir Blagojevic, and Jeffrey Chen. Self-raman nd: Yvo4 laser and electro-optic technology for space-based sodium lidar instrument. In *Solid State Lasers XXIII: Technology and Devices*, volume 8959, page 89590I. International Society for Optics and Photonics, 2014.

[2] John MC Plane, George J Flynn, Anni Määttänen, John E Moores, Andrew R Poppe, Juan Diego Carrillo-Sanchez, and Constantino Listowski. Impacts of cosmic dust on planetary atmospheres and surfaces. *Space Science Reviews*, 214(1):23, 2018.

[3] John MC Plane, Wuhu Feng, and Erin CM Dawkins. The mesosphere and metals: Chemistry and changes. *Chemical reviews*, 115(10):4497–4541, 2015.

[4] P-D Pautet, Michael J Taylor, WR Pendleton, Yucheng Zhao, Tao Yuan, R Esplin, and D McLain. Advanced mesospheric temperature mapper for high-latitude airglow studies. *Applied optics*, 53(26):5934–5943, 2014.

[5] CR Philbrick, FJ Schmidlin, KU Grossmann, G Lange, D Offermann, KD Baker, D Krankowsky, and U Von Zahn. Density and temperature structure over northern europe. *Journal of atmospheric and terrestrial physics*, 47(1-3):159–172, 1985.

[6] GG Sivjee and RM Hamwey. Temperature and chemistry of the polar mesopause oh. *Journal of Geophysical Research: Space Physics*, 92(A5):4663–4672, 1987.

[7] CY She, H Latifi, JR Yu, RJ Alvarez, RE Bills, and CS Gardner. Two-frequency lidar technique for mesospheric na temperature measurements. *Geophysical Research Letters*, 17(7):929–932, 1990.

[8] Herbert Friedman, Gaylen Erbert, and Thomas Kuklo. Sodium beacon laser system for the lick observatory. Technical report, Lawrence Livermore National Lab., CA (United States), 1995.

[9] Sebastian Rabien, Richard I Davies, Thomas Ott, Jianlang Li, Roberto Abuter, Stefan Kellner, and Udo Neumann. Test performance of the parsec laser system. In *Advancements in Adaptive Optics*, volume 5490, pages 981–989. International Society for Optics and Photonics, 2004.

[10] Yan Feng, Luke Taylor, and Domenico Bonaccini Calia. Multiwatts narrow linewidth fiber raman amplifiers. *Optics express*, 16(15):10927–10932, 2008.

[11] SA Skubchenko, MY Vyatkin, and DV Gapontsev. High-power cw linearly polarized all-fiber raman laser. *IEEE Photonics Technology Letters*, 16(4):1014–1016, 2004.

[12] Shenghong Huang, Yan Feng, Akira Shirakawa, and Ken-ichi Ueda. Generation of 10.5 w, 1178 nm laser based on phosphosilicate raman fiber laser. *Japanese Journal of Applied Physics*, 42(12A):L1439, 2003.

[13] Thomas H Jeys, AA Brailove, and Aram Mooradian. Sum frequency generation of sodium resonance radiation. *Applied optics*, 28(13):2588–2591, 1989.

[14] PF Zhu, LL Wang, CM Zhang, P Song, YX Ping, L Zhao, and Y Yao. All-solid-state side-pumped intracavity sum frequency generation yellow laser at 589 nm with the output power of 11.4 w. *Optics and Spectroscopy*, 116(3):479–482, 2014.

[15] Yuri S Kivshar. Nonlinear optics: The next decade. *Optics Express*, 16(26):22126–22128, 2008.

[16] Robert W Boyd. *Nonlinear optics*. Elsevier, 2003.

[17] Emmanuel Mimoun, Luigi De Sarlo, Jean-Jacques Zondy, Jean Dalibard, and Fabrice Gerbier. Sum-frequency generation of 589 nm light with near-unit efficiency. *Optics express*, 16(23):18684–18691, 2008.

[18] Fang Shi. Sodium laser guide star experiment with a sum-frequency laser for adaptive optics. *Publications of the Astronomical Society of the Pacific*, 113(781):366, 2001.

[19] F Hadjaj, A Belghachi, A Halmaoui, M Belhadj, and H Mazouz. Study of a fabry-perot resonator. *World Academy of Science, Engineering and Technology, International Journal of Mathematical, Computational, Physical, Electrical and Computer Engineering*, 7(12):1713–1717, 2013.

[20] Helena Jelínková. *Lasers for medical applications: diagnostics, therapy and surgery*. Elsevier, 2013.

[21] Joseph T. Verdeyen. *Laser Electronics 3rd edition*. Prentice Hall Inc., 2000.

[22] Bahaa EA Saleh and Malvin Carl Teich. *Fundamentals of photonics*. john Wiley & sons, 2019.

[23] Simon Hooker and Colin Webb. *Laser Physics*. Oxford University Press Inc., 2010.

[24] ERTAN Eryilmaz. Design and construction of a cw mode nd: Yag laser prototype. *Middle East Technical University Library. E-Thesis Archive*, 2004.

[25] Dana Z Anderson. Alignment of resonant optical cavities. *Applied Optics*, 23(17):2944–2949, 1984.

[26] Rüdiger Paschotta. Power scalability as a precise concept for the evaluation of laser architectures. *arXiv preprint arXiv:0711.3987*, 2007.

[27] Tiziano Sanvito, Francesca Zocca, Alberto Pullia, and Marco Potenza. A method for characterizing the stability of light sources. *Optics express*, 21(21):24630–24635, 2013.

[28] Alphan Sennaroglu. *Photonics and Laser Engineering*. The McGraw-Hill Companies Inc., 2010.

[29] Anthony E Siegman. How to (maybe) measure laser beam quality. In *Diode Pumped Solid State Lasers: Applications and Issues*, page MQ1. Optical Society of America, 1998.

[30] BF Hochheimer and JT Massey. Laser modes(output radiation of helium-neon gas laser describing conversion of light sources and phase variation). *APL TECHNICAL DIGEST*, 3:2–8, 1964.

[31] Darren Rand, Daniel Miller, Daniel J Ripin, and Tso Yee Fan. Cryogenic yb 3+-doped materials for pulsed solid-state laser applications. *Optical Materials Express*, 1(3):434–450, 2011.

[32] Rüdiger Paschotta. *Field guide to laser pulse generation*, volume 14. SPIE press Bellingham, 2008.

[33] Robert Goldstein. Pockels cell primer. *Laser Focus*, 34:21, 1968.

[34] Boris Denker and Eugene Shklovsky. *Handbook of solid-state lasers: materials, systems and applications*. Elsevier, 2013.

[35] JM Liu. Simple technique for measurements of pulsed gaussian-beam spot sizes. *Optics letters*, 7(5):196–198, 1982.

[36] RA Ganeev, IA Kulagin, AI Ryasnyansky, RI Tugushev, and T Usmanov. Characterization of nonlinear optical parameters of kdp, linbo3 and bbo crystals. *Optics communications*, 229(1-6):403–412, 2004.

[37] M DiDomenico Jr, JE Geusic, HM Marcos, and RG Smith. Generation of ultrashort optical pulses by mode locking the yaig: Nd laser. *Applied Physics Letters*, 8(7):180–183, 1966.

[38] Peter W Smith. Mode-locking of lasers. *Proceedings of the IEEE*, 58(9):1342–1357, 1970.

[39] U Österberg and Walter Margulis. Dye laser pumped by nd: Yag laser pulses frequency doubled in a glass optical fiber. *Optics letters*, 11(8):516–518, 1986.

[40] Marin Soljačić and John D Joannopoulos. Enhancement of nonlinear effects using photonic crystals. *Nature materials*, 3(4):211, 2004.

[41] V Berger. Nonlinear photonic crystals. *Physical review letters*, 81(19):4136, 1998.

[42] Solomon Saltiel and Yuri S Kivshar. Phase matching in nonlinear χ (2) photonic crystals. *Optics letters*, 25(16):1204–1206, 2000.

[43] Y Pastol, G Arjavalingam, GV Kopcsay, and J-M Halbout. Dielectric properties of uniaxial crystals measured with optoelectronically generated microwave transient radiation. *Applied physics letters*, 55(22):2277–2279, 1989.

[44] G Megie, F Bos, JE Blamont, and ML Chanin. Simultaneous nighttime lidar measurements of atmospheric sodium and potassium. *Planetary and Space Science*, 26(1):27–35, 1978.

[45] Yu F Arshinov, SM Bobrovnikov, Vladimir E Zuev, and VM Mitev. Atmospheric temperature measurements using a pure rotational raman lidar. *Applied Optics*, 22(19):2984–2990, 1983.

[46] Bruce M Gentry, Huailin Chen, and Steven X Li. Wind measurements with 355-nm molecular doppler lidar. *Optics letters*, 25(17):1231–1233, 2000.

[47] Rostislav V Roussev, Carsten Langrock, Jonathan R Kurz, and Martin M Fejer. Periodically poled lithium niobate waveguide sum-frequency generator for efficient single-photon detection at communication wavelengths. *Optics letters*, 29(13):1518–1520, 2004.

[48] KR Parameswaran, M Fujimura, MH Chou, and MM Fejer. Low-power all-optical gate based on sum frequency mixing in ape waveguides in ppln. *IEEE Photonics Technology Letters*, 12(6):654–656, 2000.

[49] Tadashi Nishikawa, Akira Ozawa, Yoshiki Nishida, Masaki Asobe, Feng-Lei Hong, and Theodor W Hänsch. Efficient 494 mw sum-frequency generation of sodium resonance radiation at 589 nm by using a periodically poled zn: Linbo 3 ridge waveguide. *Optics express*, 17(20):17792–17800, 2009.

[50] Randal L Schmitt and Larry A Rahn. Diode-laser-pumped nd: Yag laser injection seeding system. *Applied optics*, 25(5):629–633, 1986.

[51] SW Henderson, EH Yuen, and ES Fry. Fast resonance-detection technique for single-frequency operation of injection-seeded nd: Yag lasers. *Optics letters*, 11(11):715–717, 1986.

[52] Edward S Fry, Qiquan Hu, and Xingfu Li. Single frequency operation of an injection-seeded nd: Yag laser in high noise and vibration environments. *Applied optics*, 30(9):1015–1017, 1991.

[53] Norman P Barnes and James C Barnes. Injection seeding. i. theory. *IEEE Journal of Quantum Electronics*, 29(10):2670–2683, 1993.

[54] Yuan Xia, LiFang Du, XueWu Cheng, FaQuan Li, JiHong Wang, ZeLong Wang, Yong Yang, Xin Lin, YuChang Xun, ShunSheng Gong, et al. Development of a solid-state sodium doppler lidar using an all-fiber-coupled injection seeding unit for simultaneous temperature and wind measurements in the mesopause region. *Optics express*, 25(5):5264–5278, 2017.

[55] RS Weis and TK Gaylord. Lithium niobate: summary of physical properties and crystal structure. *Applied Physics A*, 37(4):191–203, 1985.

[56] Luis Arizmendi. Photonic applications of lithium niobate crystals. *physica status solidi (a)*, 201(2):253–283, 2004.

[57] Daryl W Preston. Doppler-free saturated absorption: Laser spectroscopy. *American Journal of Physics*, 64(11):1432–1436, 1996.